UNIVERSITÀ DI PARMA

Dottorato di Ricerca in Tecnologie dell'Informazione

XXX Ciclo

Techniques for interference mitigation in satellite communications

Coordinatore:

Chiar.mo Prof. Marco Locatelli

Tutor:

Chiar.mo Prof. Giulio Colavolpe

Dottorando: *Yuri Zanettini*

Anni 2014/2017

to my family,
to my love,
and to all my "travel mates".

Contents

Introduction **1**

1 Background **3**

1.1 Optimal MAP Symbol Detection: the BCJR Algorithm 3
1.2 Mismatched Detection 5
1.3 Frequency Packing 6

2 Advanced Receiver Architecture for DVB-S2X Systems **9**

2.1 Synchronization Aspects in DVB-S2X Satellite Systems 10
2.2 System Model 13
2.3 Adaptive Equalization in DVB-S2X Broadcast Systems 14
  2.3.1 Perfect Synchronization 16
  2.3.2 Presence of a Frequency Offset 18
2.4 Automatic Modulation Classification 18
2.5 Conclusion 27

3 Optimization of Multicarrier Satellite Broadcasting Systems **29**

3.1 Channel Model 30
3.2 Optimization of the Reference Architecture 32
  3.2.1 More Sophisticated Detection Algorithms 32
  3.2.2 Advanced Digital Predistortion Scheme 34
  3.2.3 Transmission Parameters Optimization 36
3.3 Two-Carrier Scenario 37

3.4 Six-Carrier Scenario 42
3.5 Extension to a DVB-S2X Scenario 44
3.6 Conclusions 48

4 Reception of LoRa Signals from LEO Satellites 51
4.1 LoRa Modulation 52
4.2 Detection over an AWGN Channel 60
4.3 Noncoherent Detection 63
4.4 LoRaWAN Network Protocol 63
4.5 System Simulator 68
  4.5.1 Transmission Parameters 70
  4.5.2 Channel Model 70
  4.5.3 Complex Attenuation 72
  4.5.4 Doppler Shift and Doppler Rate 72
  4.5.5 Antenna Patterns 75
  4.5.6 Link Budget 77
  4.5.7 Phase Noise 82
4.6 Receiver Performance 83
4.7 Conclusion 89

Bibliography 91

Acknowledgements 97

List of Figures

2.1 Proposed synchronization scheme. 11

2.2 Block diagram of the satellite transponder. 13

2.3 MSE before and after the equalizers for different lengths the training sequences at different values P_{sat}/N (QPSK case). 17

2.4 MSE before and after the equalizers for different lengths of the training sequences at different values of P_{sat}/N (8-PSK case). 17

2.5 MSE at $P_{\text{sat}}/N = 4.03$ dB for different lengths of the training sequence as a function of ΔfT (QPSK case). 19

2.6 MSE at $P_{\text{sat}}/N = 6.62$ dB for different lengths of the training sequence as a function of ΔfT (8-PSK case). 19

2.7 Magnitude of the fourth-order CCs computed using a moving average filter with 4320 taps when the SNR is $P_{\text{sat}}/N = 5.95$ dB. 23

2.8 Magnitude of the sixth-order CCs computed using a moving average filter with 4320 taps when the SNR is $P_{\text{sat}}/N = 5.95$ dB. 23

2.9 Fourth-order CC magnitudes of the received samples as a function of P_{sat}/N. 24

2.10 Sixth-order CC magnitudes of the received samples as a function of P_{sat}/N. 25

2.11 Modulation specific probability of wrong classification as a function of the SNR. 27

3.1 Block diagram of the satellite transponder for the two-carrier scenario. 31

3.2 Block diagram of the satellite transponder for the six-carrier scenario. 31

3.3 Block diagram of the CS receiver based on the FS-MMSE receiver. . 33

3.4 Block diagram depicting multicarrier successive digital predistortion. 35

3.5 Block diagram of the s-th iteration of the predistortion algorithm. . . 35

3.6 Schematic spectral representation of the two-carrier scenario. 37

3.7 ASE for the SUD receiver, with and without multicarrier data predistorter, compared with that in the reference case. 38

3.8 ASE for the MUD receiver, with and without multicarrier data predistorter, compared with that in the reference case. 41

3.9 Comparison between SUD and MUD receivers in the absence of memory, with and without multicarrier data predistorter. 43

3.10 Comparison between SUD and MUD receivers with $L = 1$, with and without multicarrier data predistorter. 43

3.11 Schematic spectral representation of the six-carrier scenario. 44

3.12 ASE for the SUD receiver, with and without multicarrier data predistorter, compared with that in the reference case. 45

3.13 ASE for the MUD receiver with $L = 0$, with and without multicarrier data predistorter, compared with that in the reference case. 47

3.14 Comparison between SUD and MUD receivers with $L = 0$, with and without multicarrier data predistorter. 47

3.15 Comparison between static and multicarrier DPD using a SUD receiver with $L = 0$ in a DVB-S2X scenario. 49

4.1 Function $\Gamma(t; a_k)$ for different values of a_k in the case $SF = 2$. . . . 53

4.2 Function $\Lambda(t; a_k)$ for different values of a_k in the case $SF = 2$. . . . 54

4.3 Continuous part $W_c(f)$ of the PSD of LoRa signals for $SF = 7$ and $SF = 12$. 56

4.4 Function $\Phi(t; a_k)$ for different values of a_k in the case $SF = 2$. . . 56

4.5 Function $\Psi(t; a_k)$ for different values of a_k in the case $SF = 2$. . . 58

4.6 SER for strategies (4.8) and (4.9). 62

4.7 SER comparison between strategies (4.9) and (4.12). 64

4.8 Radio physical layer structure of an uplink message. 67

4.9 CT receive slot timing. 68

4.10 A graphical representation of the cubesat FoV. 69

4.11 Graphical representation of the elevation angle θ and the distance d_u. 73

4.12 Graphical representation as seen from Nadir point: when the user sees the satellite at $\theta_{\max}$, he is in $(x_u, 0)$. 74

4.13 Doppler shift and Doppler rate values for a LEO satellite flown over the Australian region. 76

4.14 Radiation pattern of a $\lambda/4$ dipole. 76

4.15 Normalized radiation pattern of a 8-turns helical antennas. 78

4.16 Representation of the distances and angles mentioned in the derivation of the link budget. 80

4.17 Spatial distribution of C/N on the entire horizon for the European scenario when the receiving antenna is a 8-turns helical antenna. . . 81

4.18 Probability distribution of C/N on the entire horizon for the European scenario when the receiving antenna is a 8-turns helical antenna. 81

4.19 PSD of the phase noise compared to the implemented frequency response. 83

4.20 Spatial distribution of the detected packets in the satellite FoV. The borders of the considered swath are delimited in black. 85

4.21 Probability distribution of E_s/N_0 in the entire FoV of the cubesat. . 85

4.22 Percentage of successful decoding per SF for ideal impairments compensation. 86

4.23 Mean percentage of successful decoding, averaged on all SFs, for ideal impairments compensation. 86

4.24 Comparison between the receivers in terms of mean percentage of successfully detected packets per SF. 88

4.25 Comparison between different levels of amplitude interference reduction in terms of mean percentage of successfully detected packets, averaged on all SFs. 88

List of Tables

2.1 MSE before and after the equalizer when a transmission at 37 Mbaud is, compared with that in the reference case. The values have been computed in the absence of thermal noise 11
2.2 Values of P_{sat}/N corresponding approximately to packet error rate of 10^{-4} for typical MODCODs used in broadcasting transmissions. 16
2.3 MSE before and after the equalizer in a transmission on satellite channel affected by AWGN, compared with the one in the case of a quasi ISI-free transmission at 27.5 Mbaud. 18
2.4 Theoretical CCs for different modulation formats. 26

3.1 Transmission parameters for the reference case, with and without predistorter. 38
3.2 Optimized transmission parameters for a SUD receiver with $L = 0$, with and without predistorter. 39
3.3 Optimized transmission parameters for a SUD receiver with $L = 0$ and disjoint bandwidth, with and without predistorter. 40
3.4 Optimal configuration parameters for a SUD receiver with $L = 1$, with and without predistorter. 40
3.5 Best transmission parameters for a MUD receiver with $L = 0$, with and without multicarrier data predistorter. 41
3.6 Optimum transmission parameters for a MUD receiver with $L = 1$ with multicarrier predistorter. 42

3.7 Transmission parameters for the reference case, with and without predistorter. 45
3.8 Optimal transmission parameters configuration for a SUD receiver with $L = 0$, with and without multicarrier data predistorter. 46
3.9 Optimized parameters for a SUD receiver with $L = 1$, with and without multicarrier data predistorter. 46
3.10 Optimized transmission parameters for a MUD receiver with $L = 0$, with and without multicarrier data predistorter. 48

4.1 Normalized distance for different values of SF. 58
4.2 Data rates allowed by LoRaWAN for the LoRa signals. 65
4.3 Table of the possible value of radiated power density by LoRa terminal. In bold the values reserved exclusively to gateways. 66
4.4 CNR values required to achieve a BER $= 10^{-5}$ over AWGN channel, uncoded transmission and no interfering signals. 82
4.5 Probability distribution of the SF values in the scenario under study. 84

List of Publications

Journals

- G. Colavolpe, T. Foggi, M. Ricciulli, **Y. Zanettini**, “Reception of LoRa signals from LEO satellites,” manuscript under prep.
- G. Colavolpe, A. Ugolini, **Y. Zanettini**, “On multiuser detection in multicarrier DVB-S2X systems,” *IEEE Trans. on Aerospace and Electronic Systems*, manuscript under prep.
- S. Cioni, G. Colavolpe, V. Mignone, A. Modenini, A. Morello, M. Ricciulli, A. Ugolini, **Y. Zanettini**, “Transmission parameters optimization and receiver architectures for DVB-S2X systems,” *International Journal of Satellite Communications and Networking*, vol. 34, pp. 337-350, May/June 2016. Article first pubblished online: June 2015.

Conferences

- A. Ugolini, **Y. Zanettini**, A. Piemontese, A. Vanelli-Coralli and G. Colavolpe, “Efficient satellite systems based on interference management and exploitation,” *50th Asilomar Conference on Signals, Systems and Computers* (ASILOMAR 2016), Pacific Grove, California, USA, November 2016.
- A. Ugolini, M. Ricciulli, **Y. Zanettini**, G. Colavolpe, “Advanced transceiver schemes for next generation high rate telemetry,” *Proc. 8th Advanced Satel-*

lite Multimedia Systems Conference and 14th Signal Processing for Space Communications Workshop (ASMS/SPSC 2016), Palma de Mallorca, Spain, September 2016, pp. 112-119.

Patents

- G. Colavolpe, T. Foggi, M. Ricciulli, **Y. Zanettini**, “Reception of LoRa signals from LEO satellites”, assigned to Inmarsat, sent to the patent attorney for further processing.

List of Acronyms

A/D	analog-to-digital converter
AIR	achievable information rate
AMC	automatic modulation classification
APSK	amplitude/phase shift keying
ASE	achievable spectral efficiency
AWGN	additive white Gaussian noise
BCJR	Bahl-Cocke-Jelinek-Raviv
BTSs	base transceiver stations
BER	bit error rate
CCs	cyclic-cumulants
CF	cost function
CMA	constant modulus algorithm
CNR	carrier-to-noise ratio
CRC	cyclic redundancy check
CS	channel shortening
CT	client terminal
DA	data-aided
DFT	discrete Fourier transform
DPD	data predistorter

DVB-S	digital video broadcasting for satellite
DVB-S2	digital video broadcasting for satellite, 2nd generation
DVB-S2X	digital video broadcasting for satellite, 2nd generation extensions
EIRP	equivalent isotropic radiated antenna
ERP	equivalent radiated antenna
FE	front-end
FEC	forward error correction
FFT	fast Fourier transform
FoV	field of view
FP	frequency packing
FS	fractionally-spaced
FSK	frequency shift keying
GFSK	Gaussian frequency shift keying
HPA	high power amplifier
IBO	input back-off
IC	interference cancellation
ICI	interchannel interference
IMUX	input multiplexer
IoT	Internet of Things
ISI	intersymbol interference
ISM	industrial, scientific and medical
LEO	low Earth orbit
LMS	least mean squares
LoRa	long range modulation technique
LoRaWAN	long range wireless area network
MAC	media access control

MAP	maximum a posteriori
MF	matched filter
MMSE	minimum mean-square error
MODCODs	modulation and coding schemes
MSE	mean-square error
MUD	multiuser detector
OMUX	output multiplexer
PDF	probability density function
ppm	parts per million
PSD	power spectral density
PSK	phase shift keying
QAM	quadrature amplitude modulation
QPSK	quadrature phase shift keying
RRC	root-raised cosine
SBS	symbol-by-symbol
SE	spectral efficiency
SER	symbol error rate
SF	spreading factor
SNR	signal-to-noise ratio
SRRC	squared root-raised cosine
SUD	single-user detector

Introduction

SATELLITE broadband communications are a steadily growing field in the global industry, which offers a wide variety of services. Many of them, such as internet access or HDTV broadcasting, require large data rates. The need to account for this aggressive demand for higher throughput that increase every year, have pushed the research community to investigate new techniques, and to propose advanced architectures, with the aim of exploiting more efficiently the available resources.

The work presented in this thesis, hence, falls within the scope of the performance improvement of modern satellite communications systems. We will discuss and analyze several different scenarios, proposing every time the application of advanced techniques to improve the performance evaluated through a given figure of merit.

After a brief overview of some techniques and tools that will be applied to the different scenarios, provided in Chapter 1, each chapter focuses on a different problem.

Chapter 2 presents the results obtained by investigating the synchronization aspects in the extensions of the current standard for digital video broadcasting. In this scenario, aimed at the delivery of a video stream, we will propose a new non-data-aided receiver architecture that can mitigate the distorsions introduced by the increased baud rate.

Chapter 3 still focuses on signal broadcasting, but in a scenario in which multiple carriers share the same satellite payload. We will face the problem of the interference coming from the intermodulation distortions among carriers. Analyzing and comparing two different scenarios, the use of a new multicarrier digital predistorter and of advanced receiver schemes will be proposed. Moreover, we will study the potential benefits arising from the optimization of some transmission parameters joint with multiuser detection.

In Chapter 4, a feasibility study on the coverage extension of sensor networks through satellite links will be presented. We will study both the physical layer and the network protocol employed in these widely used networks. Finally, we will face the problems arising from the use of a communication standard designed for terrestrial networks on satellite links.

Chapter 1

Background

THIS chapter aims at introducing some basic concepts that will be used in the rest of the thesis. The problem of maximum a posteriori (MAP) symbol detection and multiuser detection will be addressed first. Then, we present the figure of merit that will be used for the performance analysis. Finally, a technique that allows to increase the spectral efficiency (SE) of transmission systems by properly optimizing the frequency spacing of the transmitted signals will be described.

1.1 Optimal MAP Symbol Detection: the BCJR Algorithm

In this section, we briefly review one of the most common algorithms for MAP symbol detection, the Bahl-Cocke-Jelinek-Raviv (BCJR) algorithm.

For the sake of simplicity, we consider a discrete-time linear intersymbol interference (ISI) channel, for which the received samples can be modelled as

$$y_k = \sum_{\ell=0}^{L} h_\ell x_{k-\ell} + w_k \quad k = 0, \ldots, K-1, \tag{1.1}$$

where x_k is the symbol transmitted during the k-th interval, $\{h_\ell\}_{\ell=0}^{L}$ are the coefficients of the discrete-time channel impulse response, L is the channel memory, and w_k is a complex additive white Gaussian noise (AWGN) sample with variance N_0.

This channel model can be equivalently rewritten in vector notation as

$$\mathbf{y} = \mathbf{H}\mathbf{x} + \mathbf{w},$$

where we have defined vectors $\mathbf{y} = [y_0, \ldots, y_{K-1}]^T$, $\mathbf{x} = [x_0, \ldots, x_{K-1}]^T$, and $\mathbf{w} = [w_0, \ldots, w_{K-1}]^T$, and matrix $\mathbf{H}$, with dimensions $K \times K$, which represents the ISI channel. This representation assumes the use of the Forney model for the received samples [1], but the MAP symbol detection strategy can be applied also when adopting the Ungerboeck model [2].

The MAP symbol detector computes a decision on each transmitted symbol based on the whole sequence of observed samples, as

$$\hat{x}_k = \underset{x_k}{\operatorname{argmax}}\, P(x_k|\mathbf{y}) = \underset{x_k}{\operatorname{argmax}}\, p(\mathbf{y}|x_k)P(x_k), \tag{1.2}$$

where $P(x_k)$ is the a priori probability of symbol x_k, and $p(\mathbf{y}|x_k)$ is the probability density function (PDF) of the received vector conditioned to the transmission of symbol x_k. The channel can be interpreted as a finite-state machine, with the state defined as $\sigma_k = [x_{k-1}, \ldots, x_{k-L}]$. The BCJR algorithm can effectively compute the PDF $p(\mathbf{y}|x_k)$ as

$$p(\mathbf{y}|x_k) = \sum_{\sigma_k, \sigma_{k+1}} \alpha_k(\sigma_k)\beta_{k+1}(\sigma_{k+1})p(y_k|x_k, \sigma_k). \tag{1.3}$$

Let us define the indicator function $i(x_k, \sigma_k, \sigma_{k+1})$, which is equal to one if the transition $(x_k, \sigma_k) \to x_{k+1}$ is valid and to zero otherwise. The terms $\alpha_k(\sigma_k)$ and $\beta_{k+1}(\sigma_{k+1})$ in (1.3) are the forward and backward recursion metrics of the BCJR, respectively, and they can be recursively updated as

$$\alpha_{k+1}(\sigma_{k+1}) = \sum_{x_k, \sigma_k} \alpha_k(\sigma_k)p(y_k|x_k, \sigma_k)i(x_k, \sigma_k, \sigma_{k+1})P(x_k) \tag{1.4}$$

$$\beta_k(\sigma_k) = \sum_{x_k, \sigma_{k+1}} \beta_{k+1}(\sigma_{k+1})p(y_k|x_k, \sigma_k)i(x_k, \sigma_k, \sigma_{k+1})P(x_k), \tag{1.5}$$

provided that the starting values of the recursions are properly initialized. Hence, the MAP symbol detection strategy is composed of a forward and a backward recursion, in which the quantities (1.4) and (1.5) are computed, respectively, followed by the computation of the a posteriori probabilities on the symbols, $P(x_k|\mathbf{y})$, through (1.3) and (1.2).

The BCJR algorithm is a soft-input soft-output detector, that, together with decisions on symbols, provides reliability information on said decisions, that can be exploited by a properly designed decoder. The complexity of the BCJR algorithm is proportional to $\mathcal{O}(MS)$, M being the cardinality of the transmitted symbols $\{x_k\}$ and S the cardinality of the state $\{\sigma_k\}$. The described detection algorithm can be conveniently implemented in the logarithmic domain [3].

1.2 Mismatched Detection

If we consider a channel with a channel law $p(\mathbf{y}|\mathbf{x})$, the achievable information rate (AIR) is defined as

$$I(\mathbf{x};\mathbf{y}) = \lim_{K\to\infty} \frac{1}{K}\mathbb{E}\left[\log_2 \frac{p(\mathbf{y}|\mathbf{x})}{\sum_{\mathbf{x}'} p(\mathbf{y}|\mathbf{x}')P(\mathbf{x}')}\right] \quad [\text{bit/ch. use}],$$

where $\mathbb{E}[\cdot]$ denotes the expectation operator and $P(\mathbf{x})$ is the probability distribution of the transmitted symbols. This quantity represents the highest rate achievable on a given channel with the adopted modulation format, and can be numerically computed following the technique described in [4].

This method assumes the knowledge of the channel PDF and the adoption of the optimal MAP symbol detector for it. However, if $p(\mathbf{y}|\mathbf{x})$ is unknown or the corresponding optimal detector is not available, we can compute the AIR using an arbitrary auxiliary channel law $q(\mathbf{y}|\mathbf{x})$ with the same input and output alphabets as the original channel and the corresponding optimal detector (mismatched detector). The highest rate achievable by the mismatched receiver on the original channel is [5]

$$I_R(\mathbf{x};\mathbf{y}) = \lim_{K\to\infty} \frac{1}{K}\mathbb{E}\left[\log_2 \frac{q(\mathbf{y}|\mathbf{x})}{\sum_{\mathbf{x}'} q(\mathbf{y}|\mathbf{x}')P(\mathbf{x}')}\right] \quad [\text{bit/ch. use}]$$

where $\mathbf{y}$ collects the samples from the original channel. Clearly, this detector is suboptimal for the actual channel, and hence the resulting AIR will be a lower bound on the actual one. However, this bound is achievable by that specific receiver, according to mismatched detection [4, 5].

1.3 Frequency Packing

In traditional wireless communications, orthogonal signaling is often adopted to ensure the absence of ISI and interchannel interference (ICI). However, when finite-order constellations are used, the SE of a communication system can be increased by giving up the orthogonality condition and by introducing a controlled interference into the signal.

Frequency packing is a linear modulation technique that reduces the frequency separation among adjacent carriers, with the aim to introduce ICI intentionally [6]. If the receiver is able to cope with the ICI, the efficiency of the communication system is increased. In the original papers on frequency packing signaling [6], the optimal frequency spacing is obtained as the smallest value giving no reduction of the minimum Euclidean distance with respect to the Nyquist case. This ensures that, asymptotically, the ICI-free bit error rate (BER) performance is reached when optimal detectors are used.

When considering a multicarrier system and the corresponding complex equivalent model, the recieved samples can be expressed as follows

$$y_k = \sum_{u=0}^{U-1} \sum_{\ell=0}^{L-1} h_\ell^{(u)} x_{k-\ell}^{(u)} e^{-j2\pi u\nu Fk} + w_k, \tag{1.6}$$

where the superscript $^{(u)}$ refers to the transmitted complex symbol and the channel coefficient of the u-th carrier. Parameter F is the frequency spacing that ensures orthogonality in the frequency domain and its minimum value is $F = \frac{1+\alpha}{T_s}$, where T_s is the symbol time. The extent of frequency overlapping can be tuned by choosing the compression factor $\nu \leq 1$.

Let us denote as $\mathbf{x}^{(u)} = \{x_k^{(u)}\}$ and $\mathbf{y}^{(u)} = \{y_k^{(u)}\}$ the input transmitted symbols and the received samples for the u-th carrier, respectively. The complexity of the optimal detector easily becomes unmanageable. Depending on the allowed complexity at the receiver, different strategies can be adopted for detection. For example, both ICI and ISI can be neglected and a symbol-by-symbol (SBS) detector, optimal for this auxiliary channel, adopted. The combined effect of ISI and ICI is hence modeled as a zero-mean Gaussian process independent of the additive thermal noise. This assumption is required to ensure the optimality of the SBS receiver matched to the auxiliary channel model. According to the mismatched detection theory, for the given receiver, the lower bound of the AIR for that channel can be computed as explained in Section 1.2. Since the bandwidth is a limited resource in wireless communications, we are interested to evaluate the achievable spectral efficiency (ASE), which relates to the AIR with practical transmission parameters as follows

$$\mathrm{ASE} = \frac{I_R(\mathbf{x}^{(u)}; \mathbf{y}^{(u)})}{T_s B} \quad [\mathrm{bit/s/Hz}],$$

where T_s is the symbol time and B the bandwidth of the receiver front-end filter. This lower bound is achievable for the given simplified receiver.

By applying frequency packing, we are able to improve the system performance in terms of ASE. Since we consider the ASE as the figure of merit instead of the BER performance, there is no need to keep the same Euclidean distance as in the Nyquist case, hence we can optimize the parameter ν in order to maximize the achievable SE. By reducing the frequency spacing, we accept a signal degradation, due to the increased interference, and a smaller value of AIR, but at the same time the ASE can be improved [7].

Receiver architectures more sophisticated than the SBS detector can be adopted. These receiver schemes may include an equalization stage, followed by a MAP symbol detector based on a BCJR algorithm. Further gains can be obtained by using algorithms which detect more than one carrier at a time (multiuser detection). In general, the larger the receiver complexity, the higher the gains that this technique allows to obtain.

Chapter 2

Advanced Receiver Architecture for DVB-S2X Systems

In recent years, to cope with the growing demand for high data rates, a new digital video broadcasting standard has been developed. The digital video broadcasting for satellite, 2nd generation extensions (DVB-S2X), has introduced with the aim of improving the SE through the application of innovative techniques to different stages of the transceiver architecture [8]. Compared to the previous digital video broadcasting for satellite (DVB-S) [9] and digital video broadcasting for satellite, 2nd generation (DVB-S2) [10], this new version includes also the design of new constellations, an optimization of the bandwidth and the baud rate of the transmitted signals and the adoption of advanced receiver architectures.

The reference symbol rate for DVB-S systems was 27.5 Mbaud, and this continued to be for DVB-S2, when the adopted roll-off was 0.35. Common DVB-S2 systems also operate with increased baud rates around 30 Mbaud, thanks to the additional roll-offs available in DVB-S2, even if technological evolution could allow to work with higher baud rate values. From DVB-S2 to DVB-S2X another step forward was done, furthermore reducing the roll-off until 0.1. In the case of adoption of a root-raised cosine (RRC) pulse with this roll-off value, it was demonstred that the optimal baud rate results to be 37 Mbaud [11]. However, the symbol rate increase goes hand in hand with the arise of ISI, which has to be taken into account also in the synchronization stages.

In this chapter, we discuss synchronization in high baud rate transmission systems, analysing the problems resulting from an upgrade to the new DVB-S2X standard. We propose an advanced adaptive receiver able to mitigate the distorsions on the signal, then its performance, in terms of mean-square error (MSE), is evaluated. Finally, we extend the receiver architecture employing an automatic modulation classification (AMC) technique.

2.1 Synchronization Aspects in DVB-S2X Satellite Systems

As above mentioned, one of the main differences between DVB-S2X and DVB-S2 is the introduction of a much higher baud rate at the transmitter, $R_\mathrm{s} = 37$ Mbaud precisely. This bandwidth expansion at the transmitter, jointly with the effect of input multiplexer (IMUX) and output multiplexer (OMUX) filters will introduce a significant ISI at the receiver, thus making essential the use of an equalizer at the receiver in addition to the use of a predistorter at the transmitter.

Let's focus on the receiver side. In [12], it has been found that a fractionally-spaced (FS)-minimum mean-square error (MMSE) with $N_\mathrm{tap} = 40 \div 45$ taps is a good trade-off between performance and complexity. In order to get additional insights on the impact of an increased baud rate over the system performance, we can compute the MSE between the samples and the constellation symbols at the output of the equalizer. When the optimal setting is used (i.e., $R_\mathrm{s} = 37$ Mbaud and $\alpha = 0.1$), the MSE at the equalizer output is exactly the same as we can obtain without the equalizer and a typical DVB-S2 setting ($R_\mathrm{s} = 27.5$ Mbaud and $\alpha = 0.2$). This means that the equalizer is able to effectively cope with the introduced interference. However, at the optimal baud rate, this MSE is much higher when computed before the equalizer, as shown in Tab. 2.1. The ISI before the equalizer is thus much higher, so its impact on the synchronization operations must be evaluated.

Assuming that the coarse frequency synchronization and compensation has already been performed, an evolution of the scheme proposed in [13] that implements

MOD	$R_s = 27.5$ Mbaud	$R_s = 37$ Mbaud	
		before the equalizer	after the equalizer
QPSK	0.015	0.050	0.016
8-PSK	0.016	0.051	0.018
16-APSK	0.014	0.066	0.015
32-APSK	0.016	0.081	0.017
64-APSK	0.016	0.074	0.018

Table 2.1: MSE before and after the equalizer when a transmission at 37 Mbaud is, compared with that in the reference case. The values have been computed in the absence of thermal noise

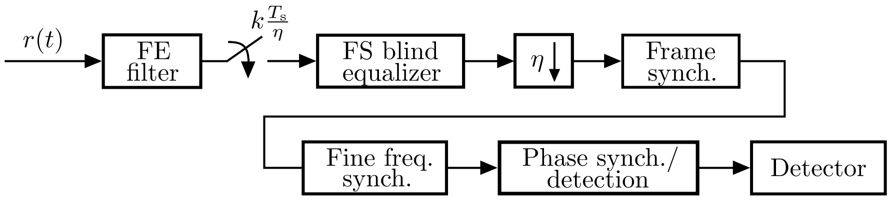

Figure 2.1: Proposed synchronization scheme.

the synchronization operations is described by the block diagram in Fig. 2.1. The considered scheme takes into account only the aspects that are actually impacted by the use of a higher baud rate—other synchronization aspects such as coarse carrier and sampling frequency offset estimations can be performed by using the digital techniques already adopted for DVB-S2 systems [14]. Among all synchronization functions, phase synchronization is not affected because it is performed in decision-directed mode and thus has to be made on the equalized samples. However, the impact of ISI on frame and fine frequency synchronization operations requires to be properly investigated. Frame synchronization can be performed by using one or more preamble blocks of the transmitted frame. Fine frequency synchronization is instead performed in data-aided (DA) mode, by using preamble and distributed pilot symbols, and thus it requires that frame synchronization is performed first. As far as the adaptation of the equalizer's coefficients is concerned, different options can be foreseen, depending on when this adaptation is made. As an example, if frame and fine frequency synchronization are available, it can be perfomed in DA mode by using both preamble and distributed pilot symbols. This is the case of the FS-MMSE equalizer adopted so far, which requires a proper DA training stage to update its coefficients. Otherwise, when the receiver does not have knowledge of the symbols used for training, as usual before performing frame synchronization, the adaptation of the equalizer's coefficients has to be performed first by using some blind algorithm.

Once the equalizer's adaptation has reached convergence, we can perform frame and fine frequency synchronization as in the absence of ISI, that is, keeping the algorithms already adopted in DVB-S2 systems, and we will obtain exactly the same performance of the case of a transmission at a baud rate of 27.5 Mbaud. At this point, the equalizer's coefficients can be further adapted in DA mode, if necessary.

Blind equalization algorithms usually have a longer acquisition time than DA algorithms. However, a longer acquisition time does not represent a problem in case of broadband systems. In the case of broadcasting systems, this adaptation can be made only once during tuning, and the information about the optimal equalizer taps can be stored with all other data related to that channel. So a longer acquisition time does not represent a problem in this case too.

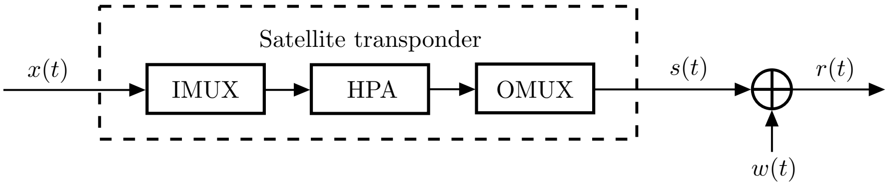

Figure 2.2: Block diagram of the satellite transponder.

2.2 System Model

We consider a single-carrier-per-transponder scenario, where each satellite transponder is assumed to work with a single carrier occupying the entire transponder bandwidth. In this case, the on-board power amplifier can operate closer to saturation and hence improve its efficiency.

The complex envelope of the signal transmitted over the carrier under consideration can be expressed as

$$x(t) = \sum_{k=0}^{K-1} a_k p(t - kT_{\mathrm{s}}),$$

where $\{a_k\}_{k=0}^{K-1}$ are the K transmitted symbols. The base pulse $p(t)$ has RRC-shaped spectrum with roll-off factor $\alpha = 0.1$, and the signal bandwidth, constrained to be limited to approximately 40 MHz, is $B = (1+\alpha)/T$. The transmitted symbols belong to an M-ary phase shift keying (PSK).

The block diagram of the satellite transponder is shown in Fig. 2.2. It includes an IMUX filter which removes the adjacent channels, a high power amplifier (HPA), and an OMUX filter aimed at reducing the spectral broadening caused by the nonlinear amplifier. The HPA AM/AM and AM/PM characteristics and the IMUX/OMUX impulse responses are described in [10], and the OMUX filter has -3 dB bandwidth equal to 38 MHz. Although the HPA is a nonlinear memoryless device, the overall system has memory due to the presence of IMUX and OMUX filters.

The received signal is further corrupted by AWGN whose low-pass equivalent $w(t)$ has power spectral density (PSD) N_0. The received signal can hence be expressed as

$$r(t) = s(t) + w(t)$$

where $s(t)$ is the signal at the output of the transponder. The front-end (FE) is composed by a low-pass filter and a sampler that works at η times the symbol rate $1/T_\mathrm{s}$, where η is the oversampling factor.

2.3 Adaptive Equalization in DVB-S2X Broadcast Systems

Many adaptive receiver structures can be used for PSK signals. We focus on a FS linear equalizer, constituted by an adaptive digital filter which takes its complex input directly from the analog-to-digital converter (A/D) at a sampling rate η/T_s. Let

$$y_k = \mathbf{c}_k^T \mathbf{r}_k$$

be the sample at the equalizer's output at time k, where

$$\begin{aligned} \mathbf{r}_k^T &= [r_k, r_{k-1}, \ldots, r_{k-N}] \\ \mathbf{c}_k^T &= [c_0, c_1, \ldots, c_{N-1}] \end{aligned}$$

are the vectors of A/D samples and equalizer's taps, respectively, and $(\cdot)^T$ denotes the transpose operator.

The most widely used algorithm for the update of the equalizer's taps is certainly the gradient descent algorithm. After a cost function (CF) has been defined, the algorithm updates the tap vector $\mathbf{c}_k$ to minimize the CF according to

$$\mathbf{c}_{k+1} = \mathbf{c}_k - \mu \nabla_{\mathbf{c}_k}(\mathrm{CF}) \tag{2.1}$$

where μ is the step-size, to be chosen as a trade-off between convergence speed and steady-state value of the CF, and $\nabla_{\mathbf{c}_k}$ represents the gradient with respect to $\mathbf{c}_k$.

The CFs that we will consider are

$$\mathrm{CF}_{\mathrm{MMSE}} = \mathbb{E}\left[\left|\mathrm{y_k} - \mathrm{a_k}\right|^2\right] \tag{2.2}$$

$$\mathrm{CF}_{\mathrm{CMA}} = \mathbb{E}\left[\left(\left|\mathrm{y_k}\right|^2 - \mathrm{R}^2\right)^2\right], \tag{2.3}$$

which are the most well-known algorithms in DA and blind mode, respectively. In the first case, the equalizer tries to minimize the mean square error between the equalizer's output and the transmitted symbols $\{a_k\}$, and for this reason, the corresponding algorithm is called MMSE algorithm. In the second case, the equalizer tries to force its output to be on the circumference of constant radius R, and it is known as constant modulus algorithm (CMA) [15].

Omitting the expectation $E[\cdot]$ in (2.2) and (2.3), i.e., by using the stochastic gradient descent algorithm, we obtain the least mean squares (LMS) version of the updating rules, and (2.1) becomes

$$\begin{aligned} \mathbf{c}_{k+1} &= \mathbf{c}_k - \mu\left(y_k - a_k\right)\mathbf{r}_k^* && \text{LMS} - \text{MMSE} \\ \mathbf{c}_{k+1} &= \mathbf{c}_k - \mu\Big(\left|y_k\right|^2 - R^2\Big)y_k\mathbf{r}_k^* && \text{LMS} - \text{CMA} \end{aligned}$$

where $(\cdot)^*$ denotes the complex conjugate. The constant R is computed as

$$R^2 = \frac{\mathbb{E}\Big[|a_k|^4\Big]}{\mathbb{E}\Big[|a_k|^2\Big]} .$$

We now compare the CMA and the DA MMSE equalizers in terms of MSE at the equalizer's output. However, in order to have a fair comparison, we have to take into account that the DA MMSE equalizer is able to recover the constant phase offset induced by the nonlinearity and the IMUX/OMUX. On the other hand, the CMA is completely insensitive to this offset, which can be recovered later by, for example, a phase synchronizer working in decision-directed mode. For this reason, before computing the MSE at the CMA output, we need to estimate and compensate this phase offset through a proper DA algorithm.

We consider typical DVB-S2 modulation and coding schemes (MODCODs) used in broadcast transmissions, limiting the cases under study to $M = 4$ and $M = 8$. The results will be reported as a function of the signal-to-noise ratio (SNR) defined as P_{sat}/N, where P_{sat} is the HPA power at saturation and $N = N_0 B_{\text{OMUX}}$ is the noise power in the OMUX bandwidth B_{OMUX}. The operating SNR values for the considered MODCODs are reported in Tab. 2.2. The number of equalizer taps is $N_{\text{tap}} = 42$, and $\eta = 2$ samples per symbol time are employed.

DVB-S	P_{sat}/N [dB]	DVB-S2	P_{sat}/N [dB]
QPSK $3/4$	4.03	QPSK $9/10$	6.42
QPSK $5/6$	5.18	8-PSK $2/3$	6.62
		8-PSK $3/4$	7.91
		8-PSK $5/6$	9.35

Table 2.2: Values of P_{sat}/N corresponding approximately to packet error rate of 10^{-4} for typical MODCODs used in broadcasting transmissions.

We will consider two scenarios. In the first one, perfect frequency synchronization, and obviously frame synchronization in case of the DA MMSE equalizer, is considered. In the second case, we will examine the robustness of the CMA equalizer in the presence of a frequency error.

2.3.1 Perfect Synchronization

Figs. 2.3 and 2.4 report, for both the CMA and DA MMSE equalizers, the MSE as a function of the number of symbols used for training, N_{t}, for quadrature phase shift keying (QPSK) with code rate $r_{\mathrm{c}} = 2/3$ and 8-PSK with $r_{\mathrm{c}} = 2/3$, for different values of P_{sat}/N. The MSE before the equalizer is also reported for comparison. Clearly, the MMSE algorithm converges faster. However, considering that DA MMSE equalizer can employ symbols in the preamble only whereas the CMA can use all data symbols, the difference in terms of absolute time is not significant. Once the CMA convergence is reached, the values of MSE are almost identical and also much lower than the 27.5 Mbaud case (see Tab. 2.3, where the MSE values are reported for all cases). These values differ from those in Tab. 2.1 because of the presence of the thermal noise.

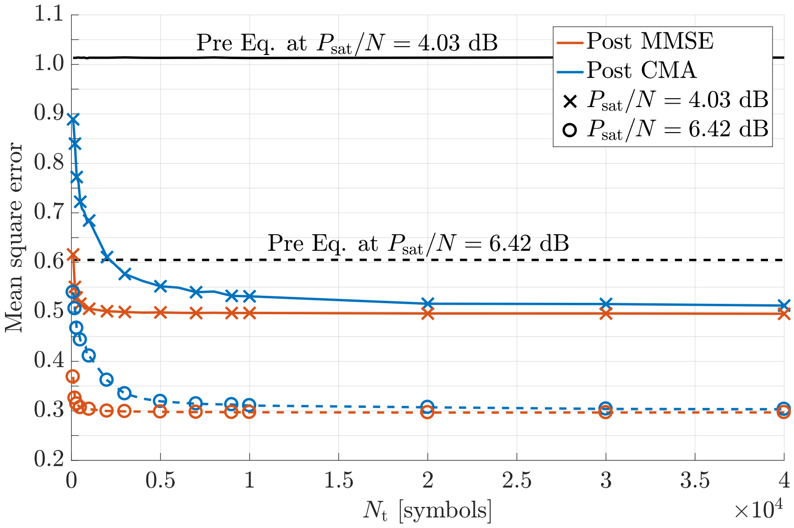

Figure 2.3: MSE before and after the equalizers for different lengths the training sequences at different values P_{sat}/N (QPSK case).

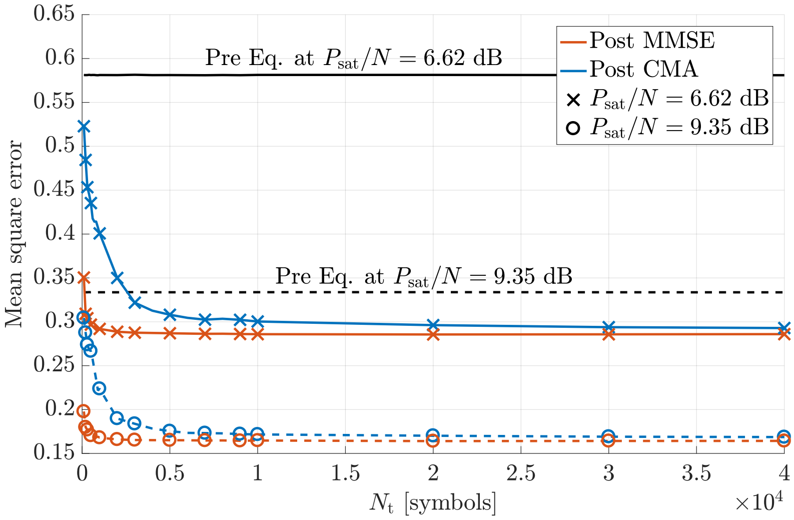

Figure 2.4: MSE before and after the equalizers for different lengths of the training sequences at different values of P_{sat}/N (8-PSK case).

MOD @ P_{sat}/N	$R_{\mathrm{s}} = 27.5$ Mbaud	$R_s = 37$ Mbaud		
		before the equalizer	after the MMSE	after the CMA
QPSK @ 4.03 dB	0.639682	1.01334	0.496292	0.499111
QPSK @ 6.42 dB	0.380915	0.60472	0.296285	0.298301
8-PSK @ 6.62 dB	0.369349	0.581187	0.285481	0.28928
8-PSK @ 9.35 dB	0.209858	0.333697	0.163921	0.166937

Table 2.3: MSE before and after the equalizer in a transmission on satellite channel affected by AWGN, compared with the one in the case of a quasi ISI-free transmission at 27.5 Mbaud.

2.3.2 Presence of a Frequency Offset

We now investigate the impact of an uncompensated frequency error on the performance of both algorithms.

While CMA error function depends on the samples modulus only, MMSE convergence is guided also by their phases. Consequently, even a small frequency offset strongly degrades the MMSE performance making it practically useless in this scenario. On the other hand, CMA is almost insensitive unless the normalized frequency offset $\Delta f T_{\mathrm{s}}$ reaches very high values. This effect is clearly described in Figs. 2.5 and 2.6, which report the MSE as a function of the normalized frequency offset, for different MODCODs and lengths of the training field used for coefficients adaptation.

2.4 Automatic Modulation Classification

Blind algorithms depend on one or more parameters, often related to the employed modulation format. The DVB-S2 standard, and its new extended version DVB-S2X, foresee the use of high-order amplitude/phase shift keying (APSK) constellations adaptively adopted according to the channel conditions. In broadcast applications, link adaptation can not be exploited, so the modulation format is fixed during the

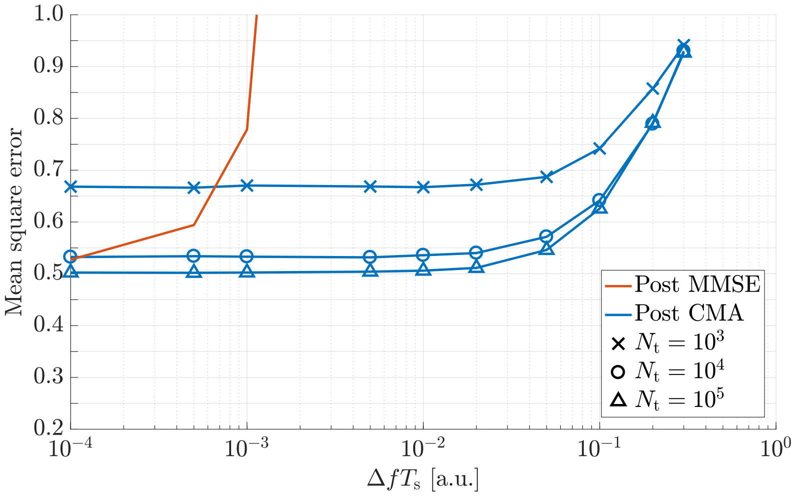

Figure 2.5: MSE at $P_{\text{sat}}/N = 4.03$ dB for different lengths of the training sequence as a function of $\Delta f T$ (QPSK case).

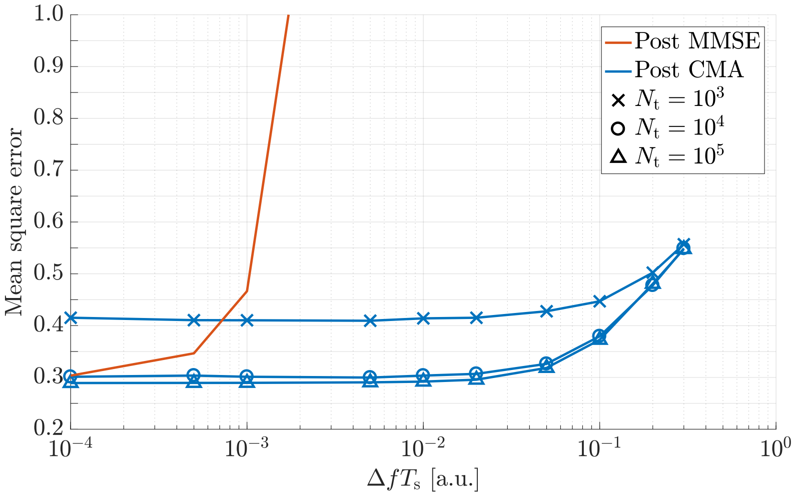

Figure 2.6: MSE at $P_{\text{sat}}/N = 6.62$ dB for different lengths of the training sequence as a function of $\Delta f T$ (8-PSK case).

overall transmission. However, during tuning, the receiver could not have a priori information about the transmitted constellation, until after synchronization stages. Synchronization is a vulnerable phase, as already above mentioned. The need to boost the convergence speed of the blind equalizer lead us to study an algorithm able to extract preliminary information from the received signal with the aim of identifying the adopted modulation format.

The problem statement is thus the following: since the transmitted symbol sequence $\mathbf{x}$ may belong to one of D known constellations, given $\mathbf{y}$ the sequence of N_s received samples, the receiver must identify the employed constellation. In the literature, one of the most famous AMC approaches is that exploiting the properties of cyclic-cumulants (CCs), which characterize the shape of the distribution of the noisy baseband samples [16]. This method is also robust in the presence of carrier phase and frequency offsets. Many research works on the AMC using the CCs approach have been published [17, 18] but most of them have taken into account PSK and quadrature amplitude modulation (QAM) only. Our aim is to extend these results, applying this type of classification to APSK constellations designed to satellite-based applications.

The simplest method for the derivation of various cumulant structures is by adopting the so-called joint cumulant generating formula of the random variables $V_1, \ldots,$ V_n, defined as

$$\mathrm{cum}(V_1, \ldots, V_n) = \sum_{\pi} (|\pi| - 1)!\, (-1)^{|\pi|-1} \prod_{U \in \pi} \mathbb{E}\left[\prod_{i \in U} V_i\right],$$

where π runs over the list of all partitions of $\{1, \ldots, n\}$ and U runs over the list of all blocks of the partition π [19]. For example, the joint cumulant of three zero-mean complex-valued stationary random variables V_1, V_2, V_3 can be written as

$$\begin{aligned}\mathrm{cum}(V_1, V_2, V_3) = {} & \mathbb{E}[V_1 V_2 V_3] - \mathbb{E}[V_1 V_2]\,\mathbb{E}[V_3] - \mathbb{E}[V_1 V_3]\,\mathbb{E}[V_2] \\ & - \mathbb{E}[V_2 V_3]\,\mathbb{E}[V_1] + 2\mathbb{E}[V_1]\,\mathbb{E}[V_2]\,\mathbb{E}[V_3]\,.\end{aligned} \tag{2.4}$$

The CCs can also be defined based on the order, which depends on the placement of the conjugation operation. For a random process V, the n-th order CCs are expressed as

$$C_{nq,V} = \mathrm{cum}(\underbrace{V, \cdots, V}_{n}, \underbrace{V^*, \cdots, V^*}_{p}) \tag{2.5}$$

Due to the symmetry of the considered signal constellations, the nth-order moments for n odd are zero and hence, using the moment to cumulant formula, it is easy to show that the nth-order CCs for n odd are also zero [20]. Let's focus on fourth and sixth-order CCs in order to study the statistics of the received signal samples. At the receiver, the signal must be oversampled in order to exploit signal cyclostationarity. Combining (2.4) and (2.5), the CCs equations can be rewritten as follows [21]

$$\begin{aligned}
C_{40,r} &= \mathrm{cum}(r, r, r, r) = \mathbb{E}\left[r^4\right] - 3\mathbb{E}\left[r^2\right]^2 \\
C_{41,r} &= \mathrm{cum}(r, r, r, r^*) = \mathbb{E}\left[r^2 \, |r|^2\right] - 3\mathbb{E}\left[r^2\right]\mathbb{E}\left[\,|r|^2\,\right] \\
C_{42,r} &= \mathrm{cum}(r, r, r^*, r^*) = \mathbb{E}\left[\,|r|^4\,\right] - \left|\mathbb{E}\left[r^2\right]\right|^2 - 2\mathbb{E}\left[\,|r|^2\,\right]^2
\end{aligned}$$

$$\begin{aligned}
C_{60,r} &= \mathrm{cum}(r, r, r, r, r, r) = \mathbb{E}\left[r^6\right] - 15\mathbb{E}\left[r^4\right]\mathbb{E}\left[r^2\right] + 30\mathbb{E}\left[r^2\right]^3 \\
C_{61,r} &= \mathrm{cum}(r, r, r, r, r, r^*) = \mathbb{E}\left[r^4 \, |r|^2\,\right] - 5\mathbb{E}\left[r^4\right]\mathbb{E}\left[\,|r|^2\,\right] \\
&\qquad - 10\mathbb{E}\left[r^2\right]\mathbb{E}\left[r^2 \, |r|^2\,\right] + 30\mathbb{E}\left[\,|r|^2\,\right]\mathbb{E}\left[r^2\right]^2 \\
C_{62,r} &= \mathrm{cum}(r, r, r, r, r^*, r^*) = \mathbb{E}\left[r^2 \, |r|^4\,\right] - \mathbb{E}\left[r^4\right]\mathbb{E}\left[r^{*2}\right] - 8\mathbb{E}\left[\,|r|^2\,\right]\mathbb{E}\left[r^2 \, |r|^2\,\right] \\
&\qquad - 6\mathbb{E}\left[r^2\right]\mathbb{E}\left[\,|r|^4\,\right] + 6\mathbb{E}\left[r^{*2}\right]\mathbb{E}\left[r^2\right]^2 \\
&\qquad + 24\mathbb{E}\left[r^2\right]\mathbb{E}\left[\,|r|^2\,\right]^2 \\
C_{63,r} &= \mathrm{cum}(r, r, r, r^*, r^*, r^*) = \mathbb{E}\left[\,|r|^8\right] - 6\mathbb{E}\left[r^2\right]\mathbb{E}\left[\,|r|^2 \, r^{*2}\right] - 9\mathbb{E}\left[\,|r|^2\right]\mathbb{E}\left[\,|r|^4\right] \\
&\qquad + 18\mathbb{E}\left[r^2\right]\mathbb{E}\left[r^{*2}\right]\mathbb{E}\left[\,|r|^2\,\right] + 12\mathbb{E}\left[\,|r|^2\,\right]^3.
\end{aligned}$$

Without loss of generality, we will assume that the constellations are normalized to have unit energy. In practice, the cumulant features are estimated from the received samples by replacing the expectation with the time average, and any scaling problem is avoided by normalizing the computed estimates:

$$\begin{aligned}\widetilde{C}_{4k,r} &= \widehat{C}_{4k,r}/\widehat{C}_{21,r}^{2} \quad k=0,1,2\\ \widetilde{C}_{6i,r} &= \widehat{C}_{6i,r}/\widehat{C}_{21,r}^{3} \quad i=0,1,2,3\end{aligned}$$

where $\widehat{C}_{nq,r}$ denotes the estimate of the nth-order/q-conjugate cumulant. If we apply these high-order statistics to a stream of received packets, whose symbols belong to different constellations, what we will observe is that some CCs are able to follow the modulation order variations. Hence, an algorithm that distinguishes the fluctuations arising from the changing of the symbol alphabet would be able to classify the transmitted constellations.

Figs. 2.7 and 2.8 demonstrate what we have just explained. The pairs of signals $\left(\widehat{C}_{40,r}, \widehat{C}_{42,r}\right)$ and $\left(\widehat{C}_{61,r}, \widehat{C}_{63,r}\right)$ have a significant variation at the time instants when a modulation switch occurs, justified by the fact that CCs theoretical values are very different from each other (see Tab. 2.4). In order to have a better understanding on which CCs have to be used and how these features can be exploited, we analyze these statistics as a function of the SNR. From Figs. 2.9 and 2.10, we observe that some CCs do not provide information on the modulation and the only signal pairs useful in the classification process are $\left(\widehat{C}_{40,r}, \widehat{C}_{42,r}\right)$ and $\left(\widehat{C}_{61,r}, \widehat{C}_{63,r}\right)$. In particular, $\widehat{C}_{40,r}$ and $\widehat{C}_{61,r}$ can be used to discriminate the QPSK constellation from those having $M > 4$ symbols. The number of rings on which symbols are placed can be identified from $\widehat{C}_{42,r}$ and $\widehat{C}_{63,r}$. Since the higher-order CCs provide a better signal discrimination especially for low values of SNR, in the following we will consider only the sixth-order statistics.

The decisions are made by minimizing the Euclidean distance between the cumulant estimate and its expected value

$$\begin{aligned}\widehat{M_1} &= \arg\min_{i\in D}\left(\left\|\widehat{C}_{61,r} - C_{61,x}\Big|_{M=i}\right\|^2\right)\\ \widehat{M_2} &= \arg\min_{i\in D}\left(\left\|\widehat{C}_{63,r} - C_{63,x}\Big|_{M=i}\right\|^2\right),\end{aligned}$$

where D is the set of candidate modulations and $C_{nq,x}\Big|_{M=i}$ is the nth-order/q conjugate cumulant computed on the APSK constellation of cardinality $M = i$ at the

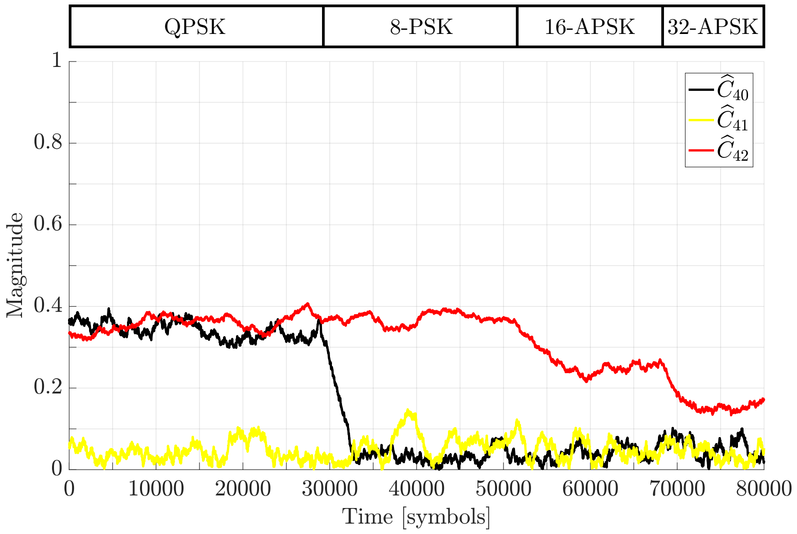

Figure 2.7: Magnitude of the fourth-order CCs computed using a moving average filter with 4320 taps when the SNR is $P_{\mathrm{sat}}/N = 5.95$ dB.

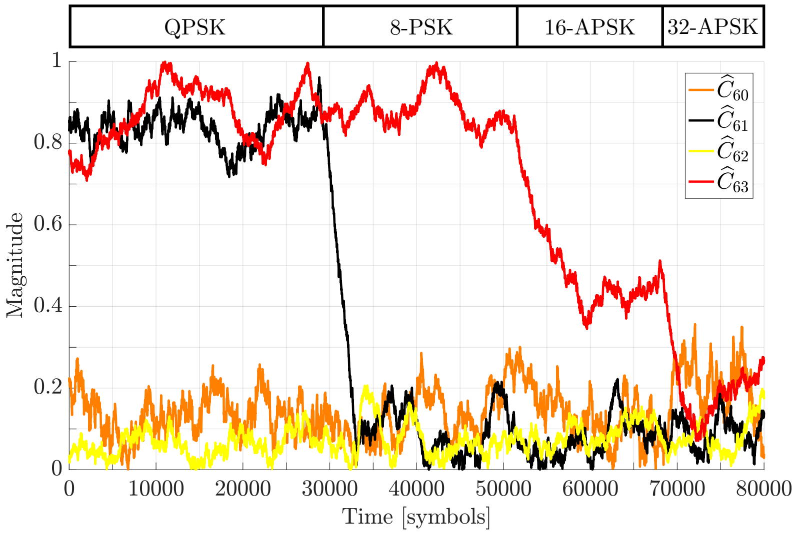

Figure 2.8: Magnitude of the sixth-order CCs computed using a moving average filter with 4320 taps when the SNR is $P_{\mathrm{sat}}/N = 5.95$ dB.

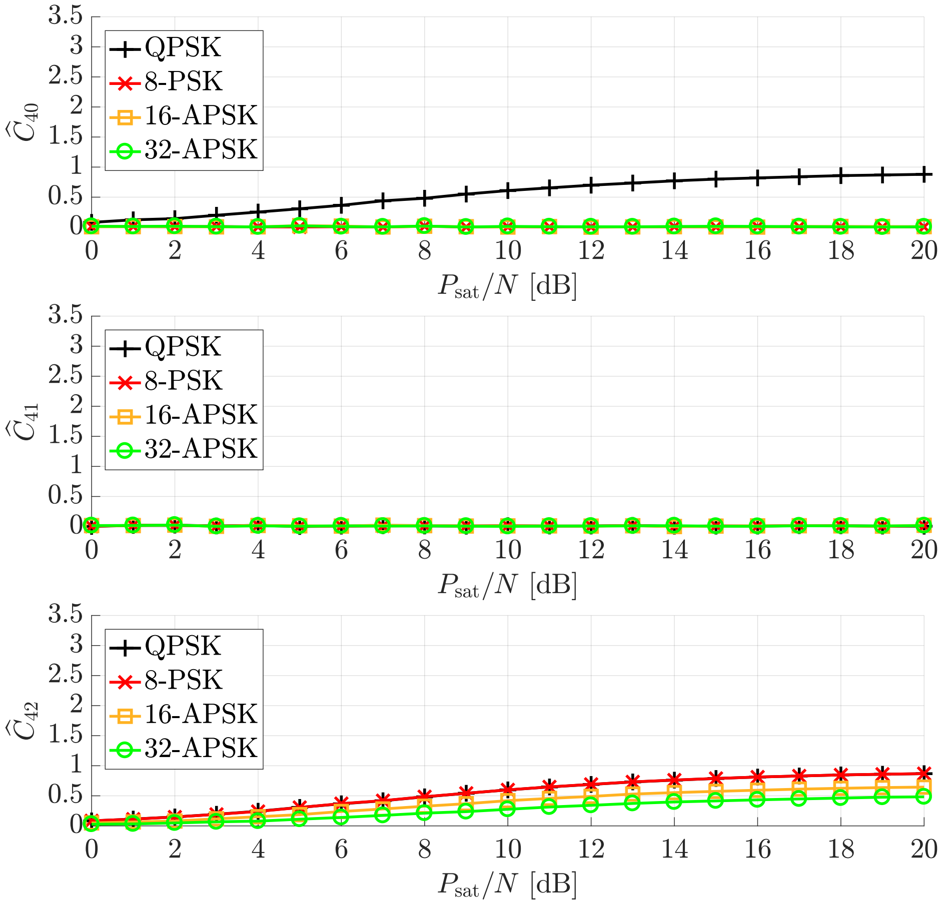

Figure 2.9: Fourth-order CC magnitudes of the received samples as a function of P_{sat}/N.

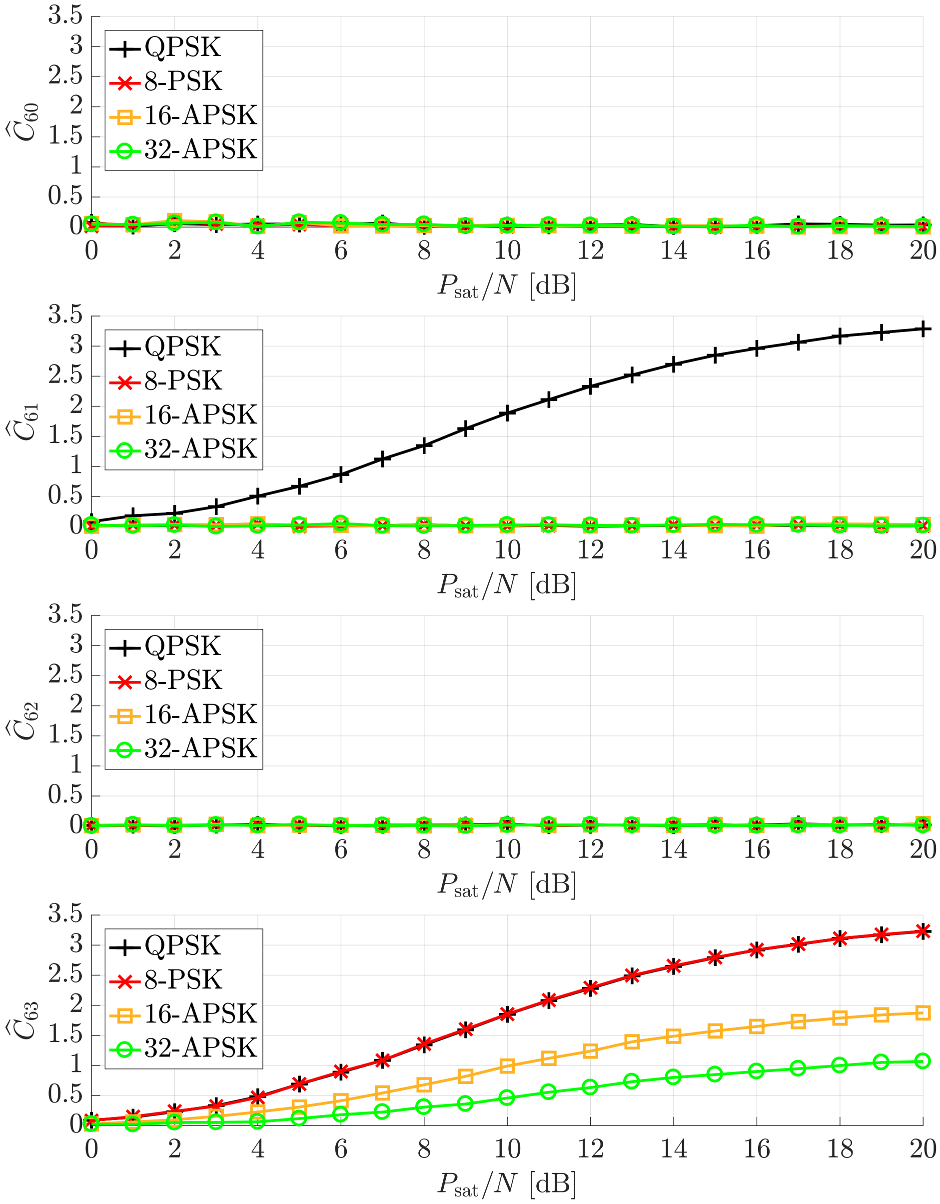

Figure 2.10: Sixth-order CC magnitudes of the received samples as a function of P_{sat}/N.

MOD	M	$\widehat{C}_{40,r}$	$\widehat{C}_{42,r}$	$\widehat{C}_{61,r}$	$\widehat{C}_{63,r}$
QAM	4	1	1	4	4
	8	0.56	0.72	1.92	2.18
	16	0.68	0.68	2.08	2.08
	32	0.61	0.62	1.79	1.8
	64	0.62	0.62	1.8	1.8
PSK	2	2	2	16	16
	4	1	1	4	4
	8	0	1	0	4
APSK	16	0	0.76	0	2.45
	32	0	0.59	0	1.48
	64	0	0.35	0	0.46

Table 2.4: Theoretical CCs for different modulation formats.

SNR P_{sat}/N. The modulation recognition is then made by combining the obtained decisions. Fig. 2.11 shows the classifier performance in terms of probability of modulation classification error. The QPSK does not appear in the results because it is considered as the basic modulation format from which starting to increase the constellation cardinality. Note that a wrong estimate does not lead to catastrophic effects on symbol detection, but only slows down the convergence of the equalizer. Since in [12] it has been demonstrated that, in the same transmission parameters configuration shown in Section 2.2, the optimal values of ASE are reached in the following SNR ranges

$$7.8 \text{ dB} \leq P_{\text{sat}}/N \leq 10 \text{ dB for 8-PSK}$$
$$P_{\text{sat}}/N \geq 10 \text{ dB for 16-APSK},$$

and within these ranges the algorithm explained above is able to distinguish with a sufficient precision between 8-PSK and 16-APSK symbols, we believe that this clas-

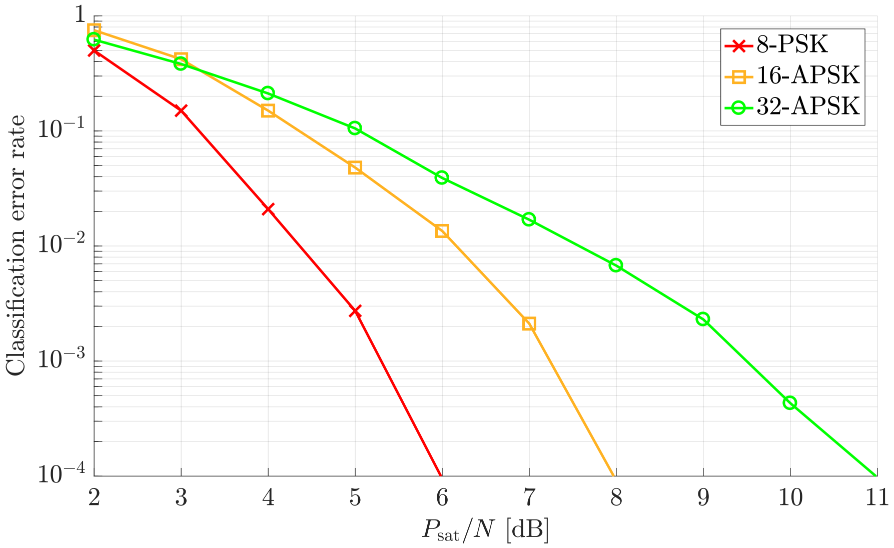

Figure 2.11: Modulation specific probability of wrong classification as a function of the SNR.

sifier can be used in order to increase the “blindness” degree of the CMA equalizer.

2.5 Conclusion

We have considered synchronization aspects and, in particular, the need of the equalizer to be trained through the transmission of a known sequence. Since it is often impossible to perform training in DA mode as required by the MMSE criterion, we applied a blind algorithm for coefficient adaptation, the CMA, which, we demonstrated, can reach the same performance as the the DA MMSE algorithm and is more robust to uncompensated frequency errors.

Then, we have exploited some statistical properties of cumulants to obtain a modulation classification, in order to improve the convergence performance of the CMA equalizer.

Chapter 3

Optimization of Multicarrier Satellite Broadcasting Systems

TRANSPARENT payload, in which data are just amplified and forwarded to the users, is the most common architecture in order to reduce costs. Carrying out all the signal processing operations to the ground, with the possibility of an update of the employed techniques with the technological advancement during the lifetime of the satellite, introduce greater degrees of freedom to enhance the link performance [22]. But in recent years, satellite communications are facing the urgent need of improving throughput to cope the higher demand for data rates in broadband and broadcast applications. This growth pushed industry to adopt remedial actions in order to compete with the quality of service offered by the terrestrial wideband networks.

Share the on-board resources among different carriers is an attractive solution that allows also to contain the satellite payload mass. In this scenario, the dedicated HPAs per carrier are replaced by a single wideband HPA which jointly amplifies multiple channels [23]. Since HPAs operate close to saturation and carriers are modulated with high-order constellations, the composite signal to be amplified is severly damaged by the intermodulation distortions among carriers. These nonlinear distortions cause the arise of ICI, which is responsible of an unacceptable performance degradation if left uncompensated, particularly when constellations include multiple concentric rings and the band guard between carriers is negligible [24].

Historically, the design of satellite communication systems has been based on *interference avoidance*. Transmission of orthogonal signals in frequency domain allows to recover data by a simple receiver structure but this approach is not optimal from an information theoretical point of view. For this, the *interference management and exploitation* paradigm is gaining ground within the research community: interference is not completely avoided by design, but a certain amount of controlled intentional interference is introduced and mitigated or exploited by the use of specifically designed transceiver architectures with the aim of enhancing system performances [25].

In this chapter, we investigate the possible improvements of the ASE in broadcast links by applying at the transmitter and at the receiver some advanced techniques that follow this latter paradigm. We analyze two different scenarios, with two and six channels per transponder, respectively. For both scenarios, we perform an optimization of the symbol rate by applying the frequency packing (FP) technique at the transmitter and more sophisticated detectors at the receiver.

3.1 Channel Model

We consider a multicarrier-per-transponder scenario, where each satellite transponder amplifies two and six band-pass signals, respectively. The complex envelope of the signal transmitted over the channel in the scenarios under study can be expressed as

$$x_2(t) = \sum_k \Big(c_k^{(1)} e^{-j\pi F t} + c_k^{(2)} e^{j\pi F t} \Big) p(t - kT_s)$$

$$\begin{aligned} x_6(t) = & \sum_k \Big(c_k^{(1)} + c_k^{(2)} e^{-j2\pi F t} + c_k^{(3)} e^{j2\pi F t} \Big) p(t - kT_s) e^{-j2\pi f_0 t} \\ & + \sum_k \Big(c_k^{(4)} + c_k^{(5)} e^{-j2\pi F t} + c_k^{(6)} e^{j2\pi F t} \Big) p(t - kT_s) e^{j2\pi f_0 t} \end{aligned}$$

where $\{c_k^{(m)}\}_{k=0}^{K-1}$ are the K symbols transmitted by the m-th user, T_s is the symbol time, and F is the frequency spacing between two adjacent carriers. The base pulse

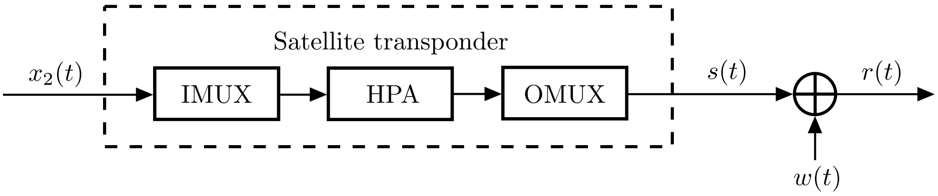

Figure 3.1: Block diagram of the satellite transponder for the two-carrier scenario.

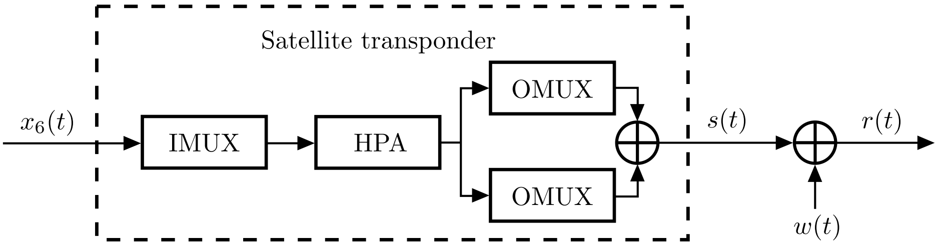

Figure 3.2: Block diagram of the satellite transponder for the six-carrier scenario.

$p(t)$ has squared root-raised cosine (SRRC)-shaped spectrum with roll-off factor α. The transmitted symbols belong to a given zero-mean complex M-ary constellation, possibly predistorted [14]. Since in the case of six carriers the signals are filtered by two different OMUX filters of bandwidth B_{OMUX} whose frequency responses are not overlapped, the two groups of three carriers are centered at the frequencies $\pm f_0 = \pm \frac{B_{\mathrm{OMUX}}}{2}$.

The block diagrams of the satellite transponder in both cases are shown in Figs. 3.1 and 3.2. The received signal is first filtered by an IMUX filter, which removes the adjacent channels, then passed through an HPA and finally filtered by a single or multiple OMUX filters with the aim of reducing the spectral broadening caused by the nonlinear amplifier. The HPA AM/AM and AM/PM characteristics and the IMUX/OMUX impulse responses are the same used in the DVB-S2 standard, described in [10]. Although the HPA is a nonlinear memoryless device, the overall system has memory due to the presence of the filters.

The received signal is further corrupted by AWGN, whose low-pass equivalent $w(t)$ has PSD $2N_0$. The received signal can be expressed as $r(t) = s(t) + w(t)$, where $s(t)$ is the signal at the output of the transponder.

3.2 Optimization of the Reference Architecture

In satellite systems, orthogonal signaling is traditionally adopted to avoid ISI and, in multi-carrier scenarios, also the interference between adjacent channels. This approach allows to reduce the complexity of the receiver architecture. With the term “reference architecture”, we hence refer to a communication system designed following the rules belonging to the *interference avoidance* paradigm, in which carriers are transmitted on non-overlapped bands, and at the receiver a simple SBS detector is sufficient to recover transmitted symbols. Nowdays, technological evolution allows to adopt more sophisticated detection and decoding techniques able to cope the undesidered or intentionally introduced interferences.

In this Section, we present some advanced techniques that can be applied to optimize this reference system, at both the transmitter and receiver sides. We consider the ASE as the figure of merit used to assess the performance of the analyzed techniques. This quantity is defined as

$$\mathrm{ASE} = \frac{I_R}{T_s B_{\mathrm{OMUX}}} \quad [\mathrm{bit/s/Hz}]$$

where I_R is the AIR computed by means of the Monte Carlo method described in [4]. When a suboptimal detector is employed, this technique gives an achievable lower bound on the actual information rate, corresponding to the information rate of the considered channel when that suboptimal detector is adopted [5]. The only condition is that the suboptimal decoder must be optimal for some arbitrary auxiliary channel. The whole investigation will be carried out under the assumption of perfect synchronization at the receiver.

3.2.1 More Sophisticated Detection Algorithms

FS-MMSE Receiver

In order to process the received signal, a sufficient statistic is extracted at the receiver

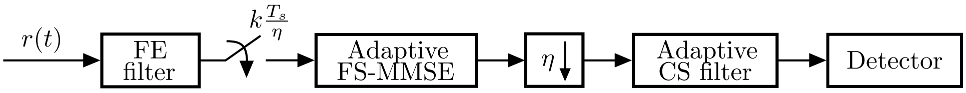

Figure 3.3: Block diagram of the CS receiver based on the FS-MMSE receiver.

by using oversampling at the output of a FE filter [26]. The distortions incurred by a signal transmitted through the satellite channel are compensated by an adaptive FS-MMSE equalizer that works at twice the symbol rate.

Since the equalizer adjusts its coefficients to track the slowly time-varying channel, the detector can be as general as possible (SBS detector or trellis-based algorithm). In the following, we will consider a filter with 42 complex taps, a good trade-off between performance and complexity, as demonstrated in [27].

Adaptive CS Receiver

Optimal trellis detection have an unmanageable complexity when the channel memory is long or constellations with high dimensions are adopted. There are two possible direction to tackle this issue:

- limiting the exploration of the original trellis and performing the detection on the visited fraction [28],
- computing a new reduced trellis which is processed at fully complexity [29].

The approach known as channel shortening (CS) is a complexity reduction technique which falls in the secondary family. Following the procedure illustrated in the work of Modenini, Rusek and Colavolpe [30], an enhanced version of the FS-MMSE that take into account also a part of channel memory, can be derived.

Fig. 3.3 shows the receiver architecture: the downsampled output of the FS-MMSE equalizer is filtered by a properly designed CS filter with the aim of reducing the complexity of the detection stage, and then BCJR algorithm performs the detection. This receiver does not rely on any specific signal model, so it is fully adaptive.

Advanced Detector

Depending on whether we want to take into account a part of the channel memory L at the receiver or not, the employed detection algorithms are a SBS detector or a BCJR algorithm [31]. The BCJR branch metrics are computed according to the adaptative CS algorithm [30].

Detection can be performed following two different strategies:

- **SUD**
  The single-user detector (SUD) returns only the information relative to a user, treating the interfering signals coming from all other users as additional thermal noise This receiver architecture has been shown to achieve excellent results in the DVB-S2X scenario [12].

- **MUD**
  A multiuser detector (MUD) returns the information on all transmitted streams [32]. This strategy improves the system performance, but at the same time, increases the receiver complexity.

3.2.2 Advanced Digital Predistortion Scheme

To mitigate the intermodulation distortions when multiple carriers share the same nonlinearity, we consider the data predistorter (DPD) described in [33]. The algorithm simulates the overall system, from data-stream modulation until the FS-MMSE equalizer at the receiver. The new complex symbol sequences to be transmitted are generated in an iterative fashion, in S iterations, minimizing the error between the undistorted symbols and the output at the previous iterations (see Fig. 3.4).

Even if the DPD updates the constellations simultaneously for all carriers during any iteration, the predistorted symbols are computed individually for each carrier. Let us focus on the s-th stage and on the u-th carrier. As shown in Fig. 3.5, an estimation of the received and equalized simbols $\hat{\mathbf{a}}_u^{(s)}$ is first computed. This estimate contains the impact of past and future of interfering data symbols from all carriers involved in the predistortion process. Modifying the symbols to be transmitted in the next stage $\mathbf{a}_u^{(s+1)}$ with a correction factor proportional to the error between the undistorted

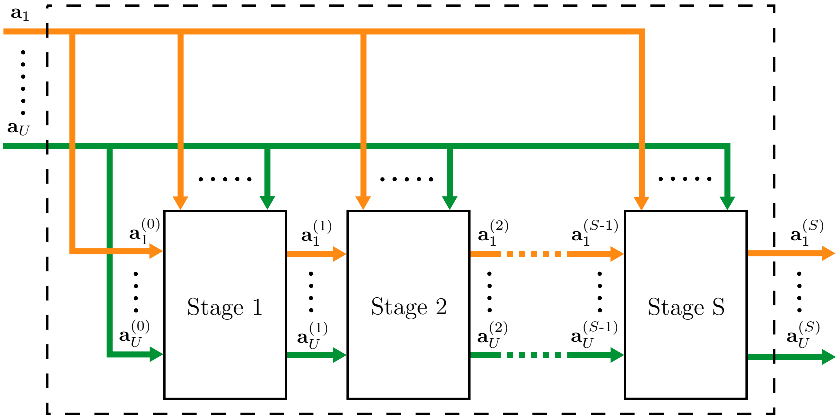

Figure 3.4: Block diagram depicting multicarrier successive digital predistortion.

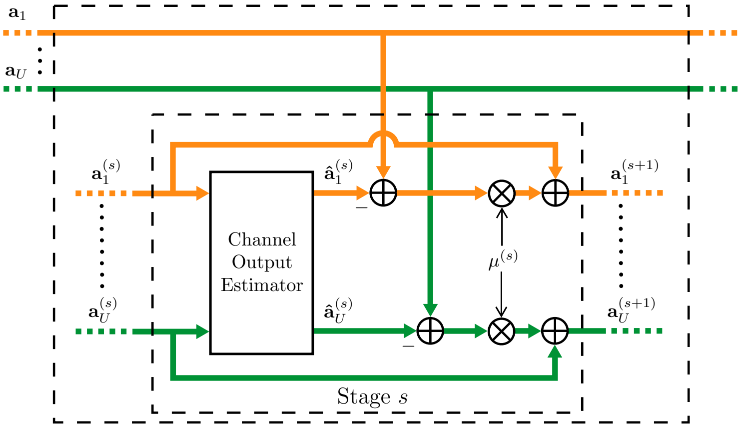

Figure 3.5: Block diagram of the s-th iteration of the predistortion algorithm.

data sequence $\mathbf{a}_u^{(0)} = \mathbf{a}_u$ and the estimator output, the successive iteration drives the distorsion error toward zero [33]. The predistortion output can be mathematically expressed as

$$\mathbf{a}_u^{(s+1)} = \hat{\mathbf{a}}_u^{(s)} - \mu^{(s)} \left(\mathbf{a}_u - \hat{\mathbf{a}}_u^{(s)} \right)$$

where $\mu^{(s)}$ is a step-size that leads the predistorter towards its convergence. The choice of this parameter has been properly made to achieve a good compromise between convergence speed and amount of residual error.

The computational complexity of the algorithm is predominantly due to two parameters involved in the channel estimation process, which approximate the filters at both the transmitter and receiver. Relaxing the complexity, performance losses occur. In the following Sections, we will neglect every forms of filters approximation, in order to present an upper bound of the ASE.

3.2.3 Transmission Parameters Optimization

It is well known that, when finite-order constellations are considered, the efficiency of the communication system can be improved by relaxing the orthogonality condition. Under these conditions, the systems are working in the domain of the *time-frequency packing* paradigm [6, 7]. In [12], it has been demonstrated that reducing the symbol interval does not guarantee any performance improvement in satellite system. On the contrary, increasing the signal bandwidth adds another degree of freedom that can be exploited to improve the SE. Since the system under study operates in the presence of adjacent signals, an excessive bandwidth increase might not be feasible, unless we use an advanced receiver. Moreover, a large frequency spacing might move signals outside of OMUX bandwidth, compromising their detection.

In light of these considerations, for a fixed predistorter complexity, we will perform a joint optimization of the predistorter step-size, the symbol rate, the frequency spacing, and the input back-off (IBO) of the amplifier, in order to derive the best transmission parameters. We consider the ASE as the figure of merit used to assess the performance of the analyzed techniques. The number of iterations that DPD must performe is set to $S = 4$, a good compromise between accuracy and complexity. All

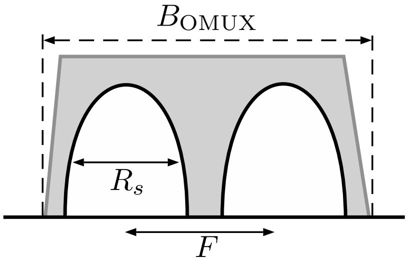

Figure 3.6: Schematic spectral representation of the two-carrier scenario.

the following results are obtained assuming a roll-off factor $\alpha = 0.1$ and the transmission of symbols from QPSK to 64-APSK when the SUD is applied, and from QPSK to 16-APSK when we use the MUD.

3.3 Two-Carrier Scenario

In Fig. 3.6 we depict a spectral representation of the scenario, in which each HPA amplifies two complex signals with symbol rate R_s Mbaud. The carriers are spaced in frequency by F MHz and the filters bandwidths are $B_{\text{IMUX}} = B_{\text{OMUX}} = 500$ MHz.

Fig. 3.7 shows the improvements arising from the parameters optimization, compared to the two alternative cases:

- **Reference**
  The reference case of signals transmitted on non overlapping bandwidths, i.e., with $R_s = 225$ Mbaud and $F = 250$ MHz (black curves). The details of these curves are reported in Tab. 3.1. A receiver based on the SUD strategy is applied for the reference case.

- **Disjoint bandwidth**
  Signals are transmitted with an optimized symbol rate R_s and with carrier spacing computed as $F = (1+\alpha)R_s$. This means that the signals cannot overlap in frequency, but we allow them to go beyond the bandwidth of the OMUX filter (orange curves). This optimization is equivalent to the completely optimized

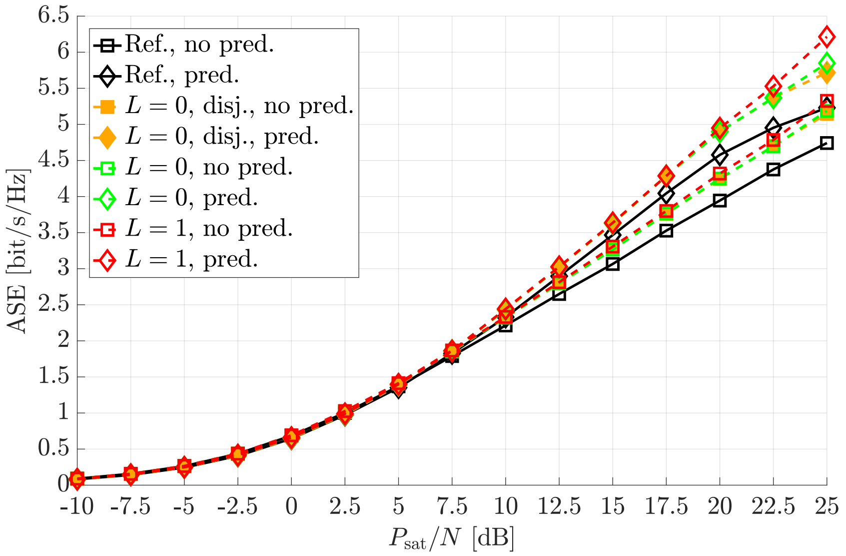

Figure 3.7: ASE for the SUD receiver, with and without multicarrier data predistorter, compared with that in the reference case.

	pred.				no pred.			
P_{sat}/N [dB]	M	R_s [Mbaud]	F [MHz]	IBO [dB]	M	R_s [Mbaud]	F [MHz]	IBO [dB]
-10	4	225	250	0	8	225	250	0
-5	8	225	250	0	8	225	250	0
0	4	225	250	0	4	225	250	0
5	8	225	250	0	8	225	250	0
10	16	225	250	3	16	225	250	3
15	64	225	250	3	64	225	250	6
20	64	225	250	6	64	225	250	9
25	64	225	250	9	64	225	250	12

Table 3.1: Transmission parameters for the reference case, with and without predistorter.

	pred.				no pred.			
P_{sat}/N [dB]	M	R_s [Mbaud]	F [MHz]	IBO [dB]	M	R_s [Mbaud]	F [MHz]	IBO [dB]
-10	8	250	225	0	8	225	200	0
-5	8	250	225	0	8	225	225	0
0	8	250	225	0	4	225	250	0
5	8	250	250	0	8	250	250	0
10	64	250	250	3	16	250	275	3
15	64	250	275	3	32	250	275	6
20	64	250	275	6	64	250	275	9
25	64	275	275	9	64	275	275	12

Table 3.2: Optimized transmission parameters for a SUD receiver with $L = 0$, with and without predistorter.

curves, but with a further constraint on the carrier spacing. Also in this case, we apply a SUD receiver.

In the case of absence of memory, the multicarrier predistorter allows to reach the same ASE as the case of undistorted symbols with a gain of almost $2 \div 3$ dB at medium-high SNR with respect to the reference case. The results obtained from the constrained optimization are almost identical to those obtained with the complete optimization. This is because the SUD achieves the best performance with signals only slightly overlapped in frequency, as we can see in Tabs. 3.2 and 3.3.

With respect to the case with $L = 0$, taking into account a larger memory ($L = 1$) we can have some further gains at high SNR due to a higher optimized symbol rate (see Tabs. 3.2 and 3.4, which report the optimized transmission parameters when a SUD receiver with $L = 0$ or $L = 1$, respectively, is employed).

When adopting the MUD strategy, the optimal configuration permits the transmission of two signals completely overlapped in frequency with symbol rate comparable to the OMUX bandwidth (see Tab. 3.5). In this case, increasing the receiver complexity does not improve the system performance, as shown in Fig. 3.8.

	pred.				no pred.			
P_{sat}/N [dB]	M	R_s [Mbaud]	F [MHz]	IBO [dB]	M	R_s [Mbaud]	F [MHz]	IBO [dB]
-10	4	225	247.5	0	4	225	247.5	0
-5	8	225	247.5	0	8	225	247.5	0
0	8	225	247.5	0	8	225	247.5	0
5	8	250	275	0	8	250	275	0
10	32	250	275	3	16	225	247.5	3
15	64	250	275	3	64	225	247.5	6
20	64	250	275	6	64	225	247.5	9
25	64	250	275	9	64	225	247.5	12

Table 3.3: Optimized transmission parameters for a SUD receiver with $L = 0$ and disjoint bandwidth, with and without predistorter.

	pred.				no pred.			
P_{sat}/N [dB]	M	R_s [Mbaud]	F [MHz]	IBO [dB]	M	R_s [Mbaud]	F [MHz]	IBO [dB]
-10	8	250	225	0	4	250	175	0
-5	8	250	225	0	8	250	225	0
0	8	250	225	0	8	250	250	0
5	8	250	250	0	8	250	250	0
10	32	250	250	3	16	275	275	3
15	64	250	275	3	64	275	275	6
20	64	275	275	6	64	275	275	9
25	64	325	325	6	64	325	350	12

Table 3.4: Optimal configuration parameters for a SUD receiver with $L = 1$, with and without predistorter.

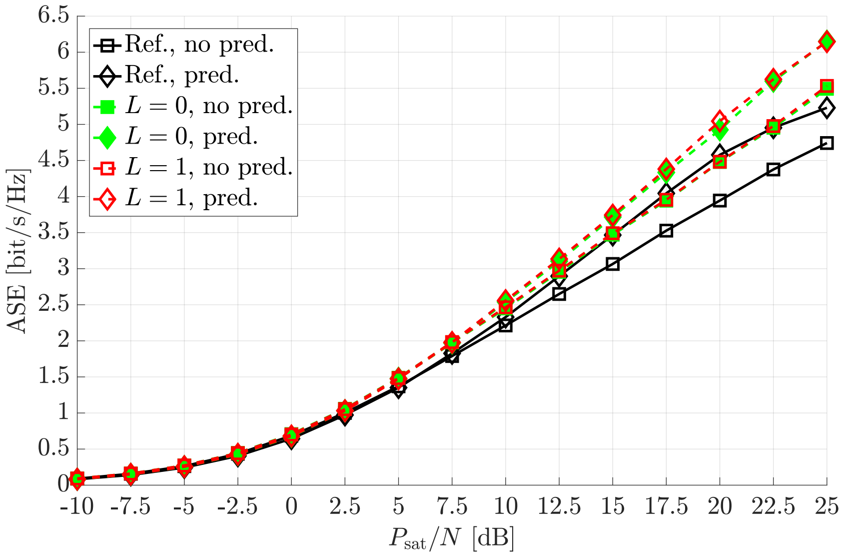

Figure 3.8: ASE for the MUD receiver, with and without multicarrier data predistorter, compared with that in the reference case.

	pred.				no pred.			
P_{sat}/N [dB]	M	R_s [Mbaud]	F [MHz]	IBO [dB]	M	R_s [Mbaud]	F [MHz]	IBO [dB]
-10	4	375	0	3	8	375	0	0
-5	4	400	0	0	8	400	0	0
0	4	500	0	3	4	500	0	0
5	4	525	0	3	4	525	0	0
10	8	525	0	0	8	525	0	3
15	16	525	0	0	8	525	0	6
20	16	525	0	3	16	525	0	9
25	16	525	0	3	16	525	0	12

Table 3.5: Best transmission parameters for a MUD receiver with $L = 0$, with and without multicarrier data predistorter.

	pred.				no pred.			
P_{sat}/N [dB]	M	R_s [Mbaud]	F [MHz]	IBO [dB]	M	R_s [Mbaud]	F [MHz]	IBO [dB]
-10	4	425	0	3	4	350	0	0
-5	4	400	0	0	8	425	0	0
0	4	525	0	3	4	475	0	0
5	4	525	0	3	4	500	0	0
10	8	500	0	0	8	525	0	3
15	16	500	0	0	8	525	0	6
20	16	550	0	0	16	525	0	9
25	16	525	0	3	16	525	0	12

Table 3.6: Optimum transmission parameters for a MUD receiver with $L = 1$ with multicarrier predistorter.

Figs. 3.9 and 3.10 compare the results illustrated above for $L = 0$ and $L = 1$, respectively. It is interesting to note from the tables how the predistorter reduces the optimal IBO of the HPA, in particular for the receiver with memory.

3.4 Six-Carrier Scenario

In this scenario, each HPA amplifies six signals, three carriers per OMUX filter. The nonlinear distortion that arises from the amplification, not only depends on the adjacent channels inside the reference OMUX, but also on the adjacent carriers. The IMUX have bandwidth $B_{\text{IMUX}} = 3$ GHz while the two OMUXs have bandwidth $B_{\text{OMUX}} = 1.5$ GHz.

Given the system architecture shown in Fig. 3.11, the following results are expressed in terms of **ASE per carriers under test**. In other words, we detect only the three channels for the OMUX under test. These results are compared with the reference case with $R_s = 450$ Mbaud and $F = 500$ MHz, corresponding to signals transmitted on non overlapping bandwidths. This configuration of parameters exactly

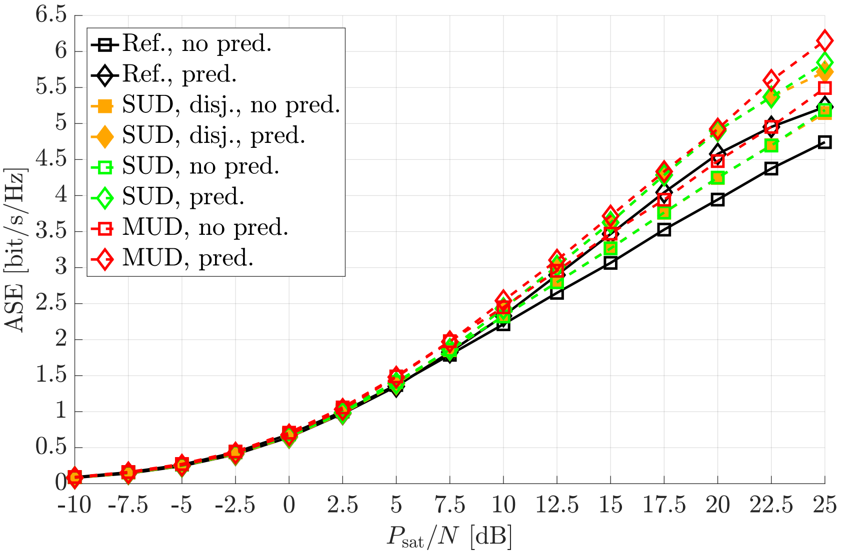

Figure 3.9: Comparison between SUD and MUD receivers in the absence of memory, with and without multicarrier data predistorter.

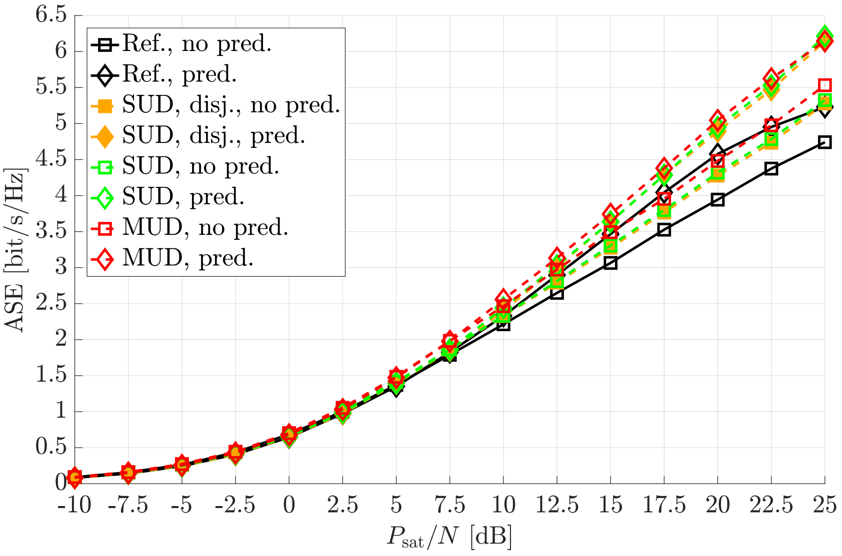

Figure 3.10: Comparison between SUD and MUD receivers with $L = 1$, with and without multicarrier data predistorter.

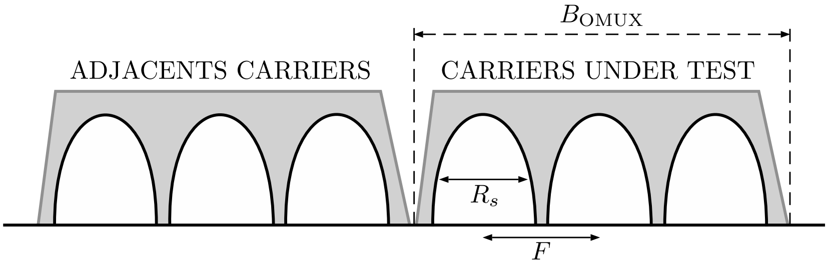

Figure 3.11: Schematic spectral representation of the six-carrier scenario.

corresponds to the optimal configuration obtained by optimizing the symbol rate R_s and constraining the signals to be on disjoint bandwidths by computing the carrier spacing as $F = (1 + \alpha)R_s$. For the sake of simplicity, we neglect the MUD receiver with memory.

Fig. 3.12 shows the ASE curves for the SUD receiver with and without memory. As we can see, there is an unperceivable gain for the receiver with memory, showing that the complexity increase necessary to apply this technique is not worth spending. This is because, in this scenario, the main impairment is ICI and not ISI. Tab. 3.7 reports the details for the reference curves, while Tabs. 3.8 and 3.9 summarize the optimized transmission parameters for a SUD receiver, with and without memory.

Significant gains over the reference architecture are possible considering a MUD receiver, as shown in Fig. 3.13, which has the best performance with signals perfectly overlapped that occupy almost the entire OMUX bandwidth (see Tab. 3.10).

Fig. 3.14 compares the results presented above in case of SBS detection at the receiver.

3.5 Extension to a DVB-S2X Scenario

The multicarrier DPD is also applied to a single-carrier DVB-S2X scenario. This scenario can be described by the same channel model illustrated in Section 3.1. In this case, only a single carrier is amplified by a HPA, and then filtered by a OMUX filter with a 3 dB bandwidth of $B_{\text{OMUX}} = 38$ MHz [10]. As a reference, we consider

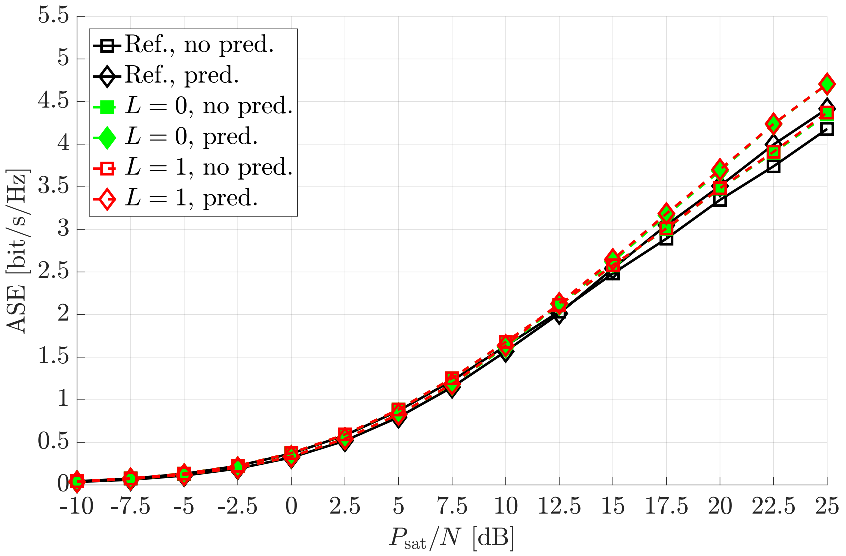

Figure 3.12: ASE for the SUD receiver, with and without multicarrier data predistorter, compared with that in the reference case.

	pred.				no pred.			
P_{sat}/N [dB]	M	R_s [Mbaud]	F [MHz]	IBO [dB]	M	R_s [Mbaud]	F [MHz]	IBO [dB]
-10	8	450	500	0	8	450	500	0
-5	4	450	500	0	8	450	500	0
0	8	450	500	3	4	450	500	0
5	8	450	500	3	8	450	500	0
10	16	450	500	3	64	450	500	3
15	64	450	500	6	64	450	500	6
20	64	450	500	6	64	450	500	9
25	64	450	500	9	64	450	500	12

Table 3.7: Transmission parameters for the reference case, with and without predistorter.

	pred.				no pred.			
P_{sat}/N [dB]	M	R_s [Mbaud]	F [MHz]	IBO [dB]	M	R_s [Mbaud]	F [MHz]	IBO [dB]
-10	8	500	350	0	8	450	500	0
-5	8	500	350	0	4	450	450	0
0	8	450	450	0	8	500	500	0
5	8	450	450	0	8	500	500	0
10	16	500	500	3	32	500	500	3
15	64	500	500	6	64	500	500	6
20	64	450	450	6	64	500	500	9
25	64	500	500	9	64	500	500	12

Table 3.8: Optimal transmission parameters configuration for a SUD receiver with $L = 0$, with and without multicarrier data predistorter.

	pred.				no pred.			
P_{sat}/N [dB]	M	R_s [Mbaud]	F [MHz]	IBO [dB]	M	R_s [Mbaud]	F [MHz]	IBO [dB]
-10	8	500	350	0	8	450	400	0
-5	8	500	350	0	4	450	450	0
0	8	450	450	0	8	450	450	0
5	8	450	450	0	32	500	500	0
10	32	450	450	3	64	500	500	3
15	64	500	500	6	64	500	500	6
20	64	450	450	6	64	500	500	9
25	64	500	500	9	64	500	500	12

Table 3.9: Optimized parameters for a SUD receiver with $L = 1$, with and without multicarrier data predistorter.

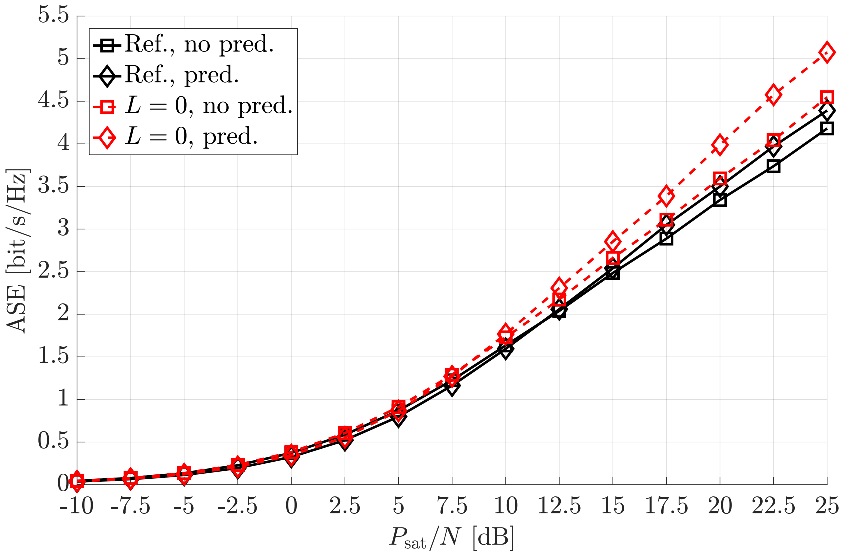

Figure 3.13: ASE for the MUD receiver with $L = 0$, with and without multicarrier data predistorter, compared with that in the reference case.

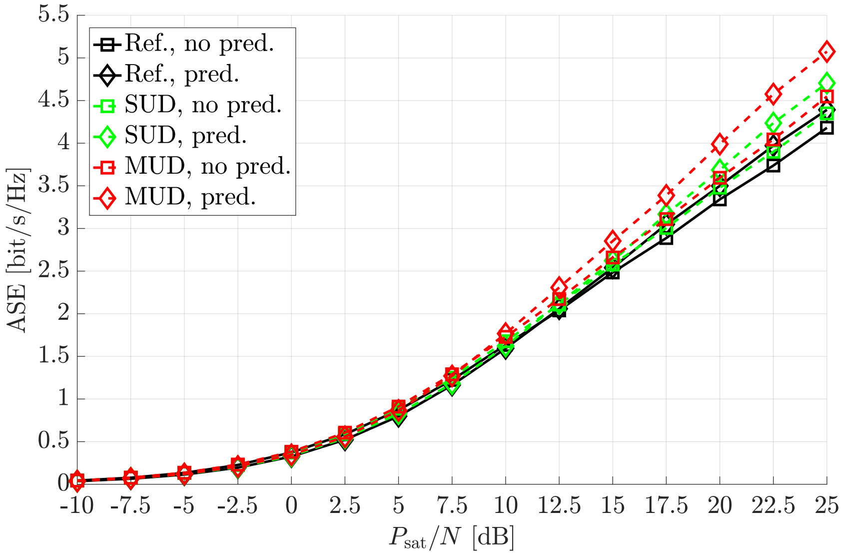

Figure 3.14: Comparison between SUD and MUD receivers with $L = 0$, with and without multicarrier data predistorter.

	pred.				no pred.			
P_{sat}/N [dB]	M	R_s [Mbaud]	F [MHz]	IBO [dB]	M	R_s [Mbaud]	F [MHz]	IBO [dB]
-10	4	900	0	0	4	900	150	0
-5	4	950	0	0	4	800	200	0
0	4	950	0	0	4	1350	0	0
5	8	1450	0	3	4	1500	0	0
10	8	1450	0	0	4	1500	0	3
15	4	1450	0	0	8	1450	0	6
20	16	1450	0	0	8	1450	0	9
25	16	1450	0	3	16	1450	0	12

Table 3.10: Optimized transmission parameters for a MUD receiver with $L = 0$, with and without multicarrier data predistorter.

a system operating at $R_s = 37$ Mbaud [11], adopting the static DPD of [14, 34]. This algorithm consists of a training phase, in which the predistorted constellation is computed based on the channel outputs.

Fig. 3.15 shows the comparison between the predistorters in terms of ASE. The cardinality of the constellation M and the IBO of the HPA have been optimized to maximise performance. For multicarrier DPD, we assuming the same complexity as previous Sections. Using the algorithm proposed by Beidas et al [33], gains of $1.5 \div 2$ dB for medium-high values of P_{sat}/N are reachable.

3.6 Conclusions

In this chapter, we have considered two multicarrier satellite systems. We have investigated the optimization of several transmission parameters with the aim of maxime the spectral efficiency. We have derived the optimal symbol rate and frequency spacing for both scenarios under study, and verified that also adopting a simple fractionally-spaced equalizer significant gains over reference architectures are possible. Perfor-

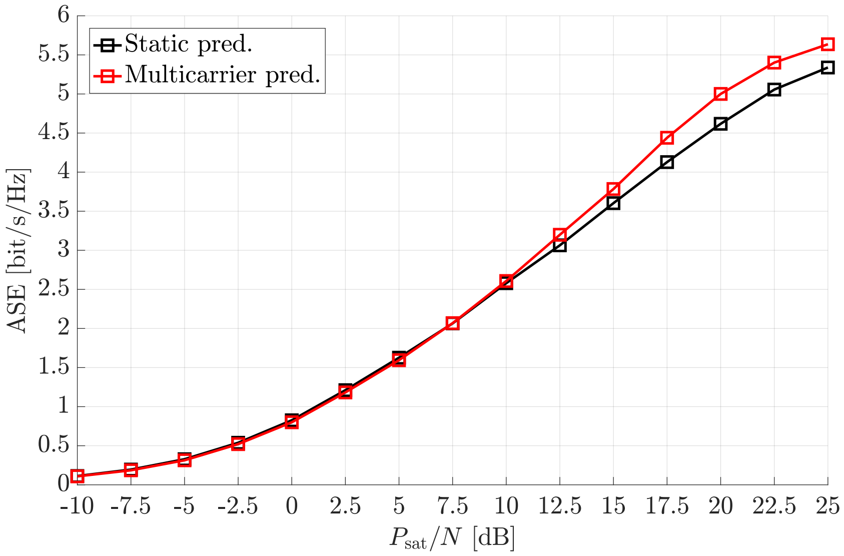

Figure 3.15: Comparison between static and multicarrier DPD using a SUD receiver with $L = 0$ in a DVB-S2X scenario.

mance of more sophisticated detection algorithms was then evaluated.

Finally, we have applied the same multicarrier predistortion algorithm and parameters optimization to a DVB-S2X system, and we have noticed a performance improvement.

Chapter 4

Reception of LoRa Signals from LEO Satellites

THE Internet of Things (IoT) is expected to revolutionize the connected world over the next years. A number of low-cost and lightweight protocols are already available for IoT devices and operate in the industrial, scientific and medical (ISM) band. These network protocols allow a new breed of smaller and cheaper devices to flourish. However, the existing IoT networks are restricted in their deployment speed by the need to install terrestrial base transceiver stations (BTSs). Furthermore, it is likely that terrestrial coverage for these networks will never extend much beyond urban areas. The use of low Earth orbit (LEO) constellations of satellites or low-cost nanosatellites (also called cubesats) could thus allow these technologies to growth in terms of deployment speed and coverage area, making possible also the signal reception from sensors used in isolated environments.

Terrestrial IoT networks are typically laid out in a star-of-stars topology in which gateways relay messages between end devices and a central network server at the backend. Nanosatellites could act as gateways, providing a link between the end-devices and the central network server where no terrestrial coverage exists. In this context, it is of a fundamental value the design of a receiver to be employed on a satellite operating in an unlicensed band as the ISM band, in which a various kind of interfering signals can be detected. The receiver must be able to reject the undesired signals and extract only messages coming from existing and unmodified IoT terrestrial terminals, which are unaware that their signals will be received by a cubesat or a traditional LEO satellite.

Focusing on the long range modulation technique (LoRa), one of the most emerging technologies in the IoT field, in this chapter, we present a feasibility study on the capability to demodulate packets transmitted by terminals belonging to a long range wireless area network (LoRaWAN) by an innovative satellite receiver. We analyze a realistic scenario, taking into account both the hardware characteristics of commercial on-the-shelf IoT devices that the radio frequency components installed on-board the cubesats.

4.1 LoRa Modulation

The complex envelope of a LoRa signal can be expressed as

$$s(t) = \sqrt{\frac{2E_s}{T_s}} \exp\left\{ j2\pi B \int_{-\infty}^{t} \left[\sum_k \Gamma(\tau - kT_s; a_k) \right] d\tau \right\} \tag{4.1}$$

where E_s is the energy per information symbol, T_s the symbol interval and a_k the transmitted symbols belonging to the alphabet $\{0, 1, \ldots, M-1\}$, being M a power of 2. The proper parameter B, whose meaning will be clarified later, can take a value in the set $\{125, 250, 500\}$ kHz, as defined by the LoRaWAN standard [35]. The function $\Gamma(\tau; a_k)$ is defined as follow

$$\Gamma(\tau; a_k) = \mathrm{mod}\left(\frac{\tau - a_k T_s/M}{T_s} \right) \mathrm{rect}\left(\frac{t}{T_s} \right) \tag{4.2}$$

where the $\mathrm{mod}(\cdot)$ function is the modulo operation in $[-1/2, 1/2)$. We define a parameter, called spreading factor (SF) in the following, as $SF = \log_2 M$. In order to obtain a LoRa signal compliant with [35], the SF must satisfy the condition

$$7 \leq SF \leq 12.$$

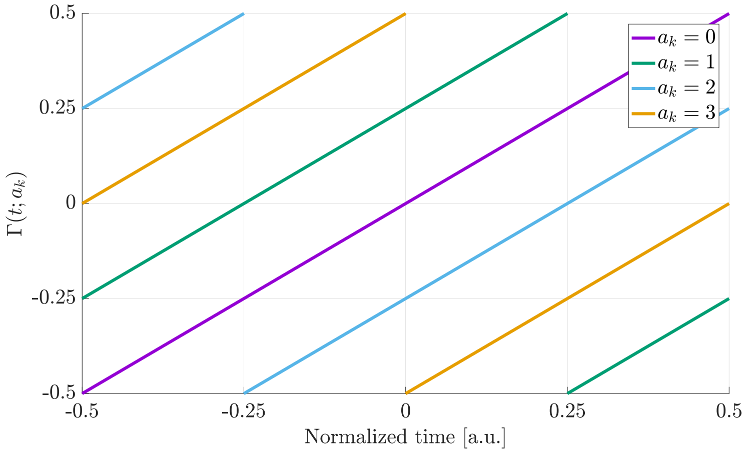

Figure 4.1: Function $\Gamma(t; a_k)$ for different values of a_k in the case $SF = 2$.

Parameters B, M, and T_s are related through the equation

$$BT = M = 2^{SF}. \tag{4.3}$$

Fig. 4.1 reports all possible functions $\Gamma(t; a_k)$ for different values of a_k in the case of $M = 4$.

This modulation format is characterized by the following important properties:

1. it has a constant envelope (and thus it is insensitive to nonlinear distortions);
2. it has a continuous phase (and thus its spectrum is compact);
3. it has no memory;
4. the occupied bandwidth is B (with good approximation).

Properties 1 and 2 are obvious from (4.1). The third property easily follows from the definition of $\Gamma(t; a_k)$. In fact, the integral of $\Gamma(t; a_k)$ is zero, no matter the value of a_k. Thus, if we consider the interval $[kT_s - T_s/2, kT_s + T_s/2)$, the phase of the complex envelope will be the same at the beginning and at the end of the interval. This modulation is thus memoryless. The shape of the function

$$\Lambda(t; a_k) = \int_{-T_s/2}^{t} \Gamma(\tau; a_k)\, d\tau$$

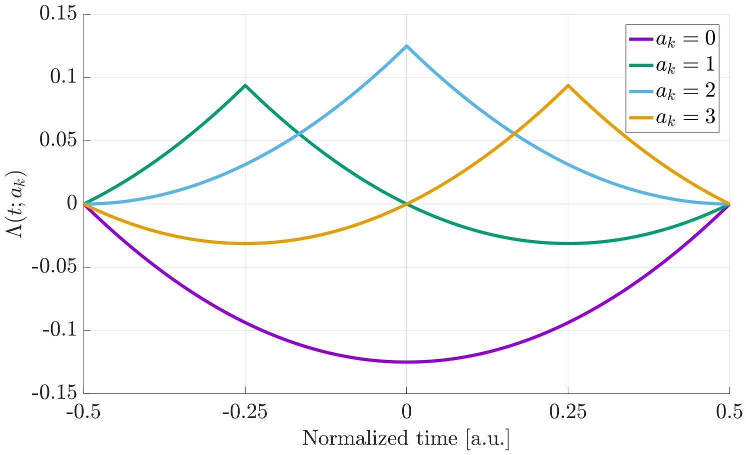

Figure 4.2: Function $\Lambda(t;a_k)$ for different values of a_k in the case $SF = 2$.

is shown in Fig. 4.2 for $M = 4$. Being the modulation memoryless, we may express its complex envelope as

$$s(t) = \sum_k \xi(t - kT_s; a_k) \tag{4.4}$$

where $\xi(t - kT_s; a_k)$ is the slice of signal, with support in $[kT_s - T_s/2, kT_s + T_s/2)$, corresponding to symbol a_k and has expression

$$\xi(t-kT_s;a_k)=\sqrt{\frac{2E_{\mathrm{s}}}{T_s}}\exp\left\{j2\pi B\int_{kT_s-T_s/2}^{\min(t,kT_s+T_s/2)}\Gamma(\tau - kT_s;a_k)\,d\tau\right\}\mathrm{rect}\left(\frac{t}{T_s}\right).$$

A closed-form expression of the PSD $W_s(f)$ of a signal that can be expressed in the form (4.4) exists [36]. It is composed of a continuous part $W_c(f)$ and a discrete part $W_\delta(f)$ made of a modulated Dirac delta train

$$W_s(f) = W_c(f) + W_\delta(f),$$

where

$$W_c(f) = \frac{1}{T_s}\left[\frac{1}{M}\sum_{a_k}\left|\Xi(f;a_k)\right|^2 - \left|\frac{1}{M}\sum_{a_k}\Xi\left(f;a_k\right)\right|^2\right]$$

and

$$W_\delta(f) = \frac{1}{M^2 T_s^2} \sum_{n=-\infty}^{\infty} \left| \sum_i \Xi\left(\frac{n}{T_s}; a_i\right) \right|^2 \delta\left(f - \frac{n}{T_s}\right)$$

having denoted by $\Xi(f; a_k)$ the Fourier transform of $\xi(t; a_k)$ whose closed-form expression is

$$\begin{aligned}\Xi(f; a_k) = \sqrt{\frac{E_s T_s}{M}} \exp\left\{ j2\pi B \left(\frac{3T_s}{8} - \frac{T_s}{2} \left(\frac{a_k}{M} + \left(\frac{a_k}{M} - 1 + \frac{f}{B} \right)^2 \right) \right) \right\} \\ \cdot \left\{ Z\left[\sqrt{2M} \left(\frac{1}{2} - \frac{f}{B} \right) \right] - Z\left[\sqrt{2M} \left(-\frac{a_k}{M} + \frac{1}{2} - \frac{f}{B} \right) \right] \right\} + \\ + \sqrt{\frac{E_s T_s}{M}} \exp\left\{ j2\pi B \left(-\frac{T_s}{8} + \frac{T_s}{2} \left(\frac{a_k}{M} + \left(\frac{a_k}{M} + \frac{f}{B} \right)^2 \right) \right) \right\} \\ \cdot \left\{ Z\left[\sqrt{2M} \left(-\frac{a_k}{M} + \frac{1}{2} - \frac{f}{B} \right) \right] - Z\left[\sqrt{2M} \left(-\frac{1}{2} - \frac{f}{B} \right) \right] \right\}\end{aligned}$$

where $Z(\cdot) = C(\cdot) + jS(\cdot)$ and the Fresnel integrals are defined as follow [37]

$$C(x) = \int_0^x \cos\left(\frac{\pi}{2} y^2\right) dy \qquad S(x) = \int_0^x \sin\left(\frac{\pi}{2} y^2\right) dy.$$

Fig. 4.3 reports the continuous part $W_c(f)$ of the PSD of LoRa signals for $SF = 7$ and $SF = 12$. As shown in Fig. 4.3, a significant portion of the power is in the frequency range $\left[-\frac{B}{2}, \frac{B}{2}\right]$. We can thus conclude that the bandwidth of the corresponding passband signal is B.

From the observation of Fig. 4.1, we can easily understand that we may express

$$\Gamma(t; a_k) = \Gamma(t; 0) + \Phi(t; a_k)$$

i.e., as a first contribution which is the value of $\Gamma(t; a_k)$ corresponding to symbol $a_k = 0$, thus common to all terms, plus a second term which depends on a_k and can be expressed as

$$\Phi(t; a_k) = \begin{cases} -\frac{a_k}{M} + 1 & \text{for } -\frac{T_s}{2} \leq t \leq -\frac{T_s}{2} + a_k \frac{T_s}{M} \\ -\frac{a_k}{M} & \text{for } -\frac{T_s}{2} + a_k \frac{T_s}{M} < t \leq \frac{T_s}{2} \end{cases}. \tag{4.5}$$

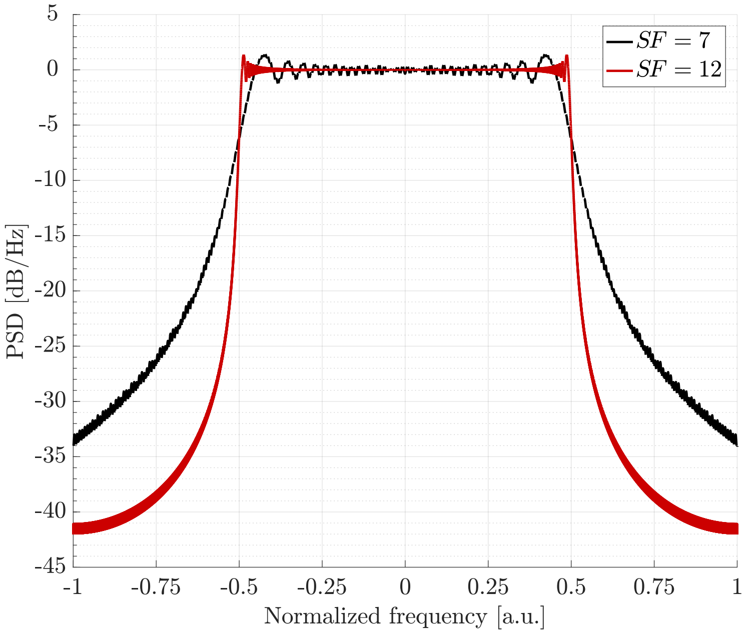

Figure 4.3: Continuous part $W_c(f)$ of the PSD of LoRa signals for $SF = 7$ and $SF = 12$.

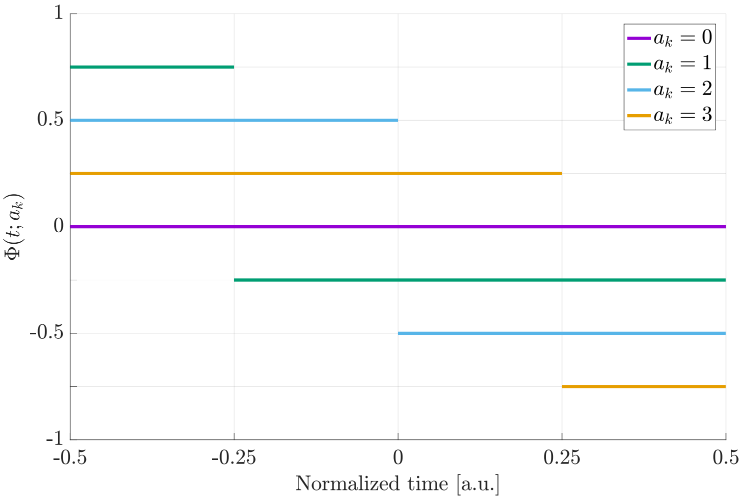

Figure 4.4: Function $\Phi(t; a_k)$ for different values of a_k in the case $SF = 2$.

The term $\Phi(t;a_k)$ is thus a piecewise constant and is shown in Fig.4.4 for different values of a_k in the case of $SF = 2$.

Finally, the complex envelope of a LoRa signal in the generic interval $[kT_s - T_s/2, kT_s + T_s/2)$ can be equivalently expressed as

$$\xi(t-kT_s;a_k) = \xi(t-kT_s;0)\exp\left\{j2\pi B\int_{-kT_s-T_s/2}^{t}\Phi\left(\tau-kT_s;a_k\right)d\tau\right\}$$

where

$$\xi(t-kT_s;0) = \sqrt{\frac{2E_\mathrm{s}}{T_s}}\exp\left\{j2\pi B\int_{kT-T_s/2}^{t}\Gamma\left(\tau-kT_s;0\right)d\tau\right\} \tag{4.6}$$

is the slice of signal corresponding to $a_k = 0$ and is a term whose phase quadratically depends on t (see Fig. 4.1). This is thus an up-chirp signal. We can define

$$\Psi(t-kT_s;a_k) = 2\pi B\int_{-kT_s-T_s/2}^{t}\Phi(\tau-kT;a_k)d\tau$$

obtaining

$$\xi(t-kT_s;a_k) = \xi(t-kT_s;0)\exp\left\{j\,\Psi(t-kT_s;a_k)\right\}.$$

The shape of $\Psi(t;a_k)$ is shown in Fig. 4.5 for $SF = 2$.

Let us consider again the generic interval $[kT_s - T_s/2, kT_s + T_s/2)$. The slices $\xi(t-kT;a_k)$ corresponding to different symbols a_k are not orthogonal. This can be simply verified by computing the $M \times M$ matrix $\boldsymbol{A}$ whose elements are defined as

$$A_{i,\ell} = \frac{T_s}{2E_s}\int_{kT_s-T_s/2}^{kT_s+T_s/2}\xi(t-kT_s;a_k=i)\xi^*(t-kT_s;a_k=\ell)\,dt.$$

If the slices $\xi(t-kT_s;a_k)$ were orthogonal, $\boldsymbol{A}$ would be the identity matrix. So in order to understand how far is this matrix from the identity one, we computed the normalized distance $\frac{1}{M}\left\|\boldsymbol{A}-\boldsymbol{I}\right\|_\mathrm{F}$ where $\boldsymbol{I}$ is the $M \times M$ identity matrix and $\|\cdot\|_\mathrm{F}$ is the Frobenius norm. The values are reported in Tab. 4.1 for different values of SF. We may thus conclude that the slices $\xi(t-kT;a_k)$ are not strictly orthogonal but can be approximated as such.

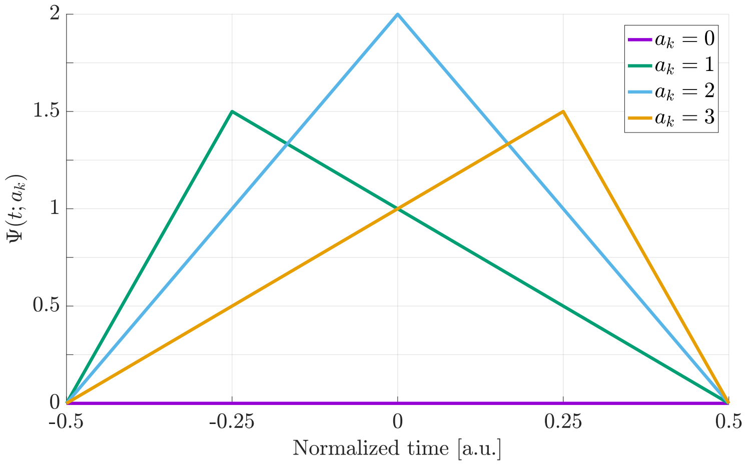

Figure 4.5: Function $\Psi(t; a_k)$ for different values of a_k in the case $SF = 2$.

SF	$\frac{1}{M}\|\boldsymbol{A} - \boldsymbol{I}\|_{\mathrm{F}}$	SF	$\frac{1}{M}\|\boldsymbol{A} - \boldsymbol{I}\|_{\mathrm{F}}$
3	$1.3 \cdot 10^{-1}$	8	$9.4 \cdot 10^{-3}$
4	$7.8 \cdot 10^{-2}$	9	$5.5 \cdot 10^{-3}$
5	$4.6 \cdot 10^{-2}$	10	$3.2 \cdot 10^{-3}$
6	$2.7 \cdot 10^{-2}$	11	$1.9 \cdot 10^{-3}$
7	$1.6 \cdot 10^{-2}$	12	$1.1 \cdot 10^{-3}$

Table 4.1: Normalized distance for different values of SF.

We said that signal $s(t)$ has approximately a bandwidth $B/2$. It can be thus reconstructed from its samples when using a sampling frequency $F_s = B = M/T_s$. Without loss of generality, we can consider the interval $[-T_s/2, T_s/2)$ and thus the transmission of symbol a_0. The M samples of the complex envelope are

$$\xi\left(\frac{\ell T_s}{M}; a_0\right) = \xi\left(\frac{\ell T_s}{M}; a_0 = 0\right) \exp\left\{j\,\Psi\left(\frac{\ell T_s}{M}; a_0\right)\right\}, \qquad \ell = -\frac{M}{2}, \ldots, \frac{M}{2} - 1.$$

By unwrapping the phase $\Psi\left(\frac{\ell T_s}{M}; a_0\right)$, it can be easily verified that

$$\exp\left\{j\,\Psi\left(\frac{\ell T_s}{M}; a_0\right)\right\} = \exp\left\{-j\frac{2\pi}{M}a_0\left(\ell + \frac{M}{2}\right)\right\}, \qquad \ell = -\frac{M}{2}, \ldots, \frac{M}{2} - 1$$

and thus

$$\xi\left(\frac{\ell T_s}{M}; a_0\right) = \xi\left(\frac{\ell T_s}{M}; a_0 = 0\right) \exp\left\{-j\frac{2\pi}{M}a_0\left(\ell + \frac{M}{2}\right)\right\}, \ell = -\frac{M}{2}, \ldots, \frac{M}{2} - 1$$

or, equivalently

$$\xi_n(a_0) = \xi_n(a_0 = 0) \exp\left\{-j\frac{2\pi}{M}a_0 n\right\}, \quad n = 0, 1, \ldots, M-1 \tag{4.7}$$

having defined

$$\xi_n(a_0) = \xi\left(\frac{\ell T_s}{M}; a_0\right).$$

In other word, we can write the samples as the product of an up-chirp signal, common to all signals, and a term whose phase is linearly decreasing with a slope depending on the transmitted symbol. These discrete-time samples are, this time, orthogonal. In fact

$$\sum_{n=0}^{M-1} \xi_n(a_0 = i)\xi_n^*(a_0 = \ell) = \begin{cases} M & i = \ell \\ 0 & i \neq \ell \end{cases}.$$

It is important to notice that if we sample with a lower or higher sample frequency, this property no more holds, i.e., we can still write the samples as the product of an up-chirp signal, common to all signals, and a second term depending on the transmitted symbol, but this time the phase of this second term is no more linearly decreasing.

4.2 Detection over an AWGN Channel

Let us assume that an uncoded LoRa signal is transmitted over an AWGN channel and that ideal synchronization has been performed. Without loss of generality, since the modulation is memoryless, as discussed in the previous section, we can consider the interval $[-T_s/2, T_s/2)$ focusing on detection of symbol a_0 only. The complex envelope of the received signal can thus be expressed as

$$r(t) = \xi(t; a_0) + w(t)$$

where $w(t)$ is the complex envelope of the additive white Gaussian noise. $w(t)$ is a complex Gaussian noise process with independent real and imaginary components having zero mean and PSD N_0.

From a conceptual point of view, optimal detection of LoRa signals can be performed through the following MAP detection strategy [38][1]

$$\hat{a}_0 = \underset{a_0}{\operatorname{argmax}} \operatorname{Re}\big\{z(a_0)\big\} \tag{4.8}$$

having defined

$$z(a_0) = \int_{-T_s/2}^{T_s/2} r(t)\xi^*(t; a_0)\, dt$$

i.e., $z(a_0)$ is obtained by sampling the received signal $r(t)$ filtered through a filter matched to $\xi(t; a_0)$ (matched filter (MF)). We can thus conclude that a sufficient statistic can be obtained through a bank of $M = 2^{SF}$ MFs to all possible waveforms $\xi(t; a_0)$.

Although this receiver is quite simple from a conceptual point of view, it can hardly be implemented when M grows. Let us consider a digital implementation of the bank of M MFs. In practical receivers, an approximated set of sufficient statistics is obtained through the technique described in [26]. It is assumed that the LoRa low-pass equivalent is band-limited with bandwidth $B/2$, although this is not strictly true as discussed in the previous section. The approximated statistics can be obtained

---

[1] This detection strategy has been obtained by exploiting the fact that $\xi(t; a_0)$ has a constant envelope.

by sampling the received signal prefiltered by means of an ideal analog lowpass filter having bandwidth $B/2$. The use of an ideal filter ensures that the noise samples are independent and identically distributed complex Gaussian random variables with independent components. As discussed in the previous section, we need at least M samples to represent the transmitted signal in the interval $[-T_s/2, T_s/2)$. The complexity related to the implementation of M MFs is thus proportional to M^2.

A significant complexity reduction can be obtained by exploiting (4.7). In fact, we can express the received samples as

$$r_n = \xi_n(a_0 = 0)e^{-j\frac{2\pi}{M}a_0 n} + w_n$$

where w_n are additive white Gaussian noise samples [26]. We can thus remove the up-chirp signal by computing

$$y_n = r_n^* \xi_n(a_0 = 0) = e^{j\frac{2\pi}{M}a_0 n} + w'_n$$

where w'_n are still additive white Gaussian noise samples since the up-chirp signal has a constant amplitude and does not modify the noise statistics. The optimal MAP detection strategy based on these samples can be expressed as

$$\hat{a}_0 = \operatorname*{argmax}_{a_0} \operatorname{Re}\left\{ \sum_{n=0}^{M-1} y_n e^{-j\frac{2\pi}{M}a_0 n} \right\}. \tag{4.9}$$

Looking at (4.9), we can recognize that the strategy can be expressed as

$$\hat{a}_0 = \operatorname*{argmax}_{k} \operatorname{Re}\{Y_k\}$$

having defined

$$Y_k = \sum_{n=0}^{M-1} y_n e^{-j\frac{2\pi}{M}kn}$$

as the discrete Fourier transform (DFT) of samples y_n. It can be thus efficiently computed through the fast Fourier transform (FFT) with complexity $M\log_2 M = M\cdot SF$.

The error probability of strategy (4.9) is known in an analytical form. In fact, since the discrete-time waveforms are orthogonal, the symbol error probability is

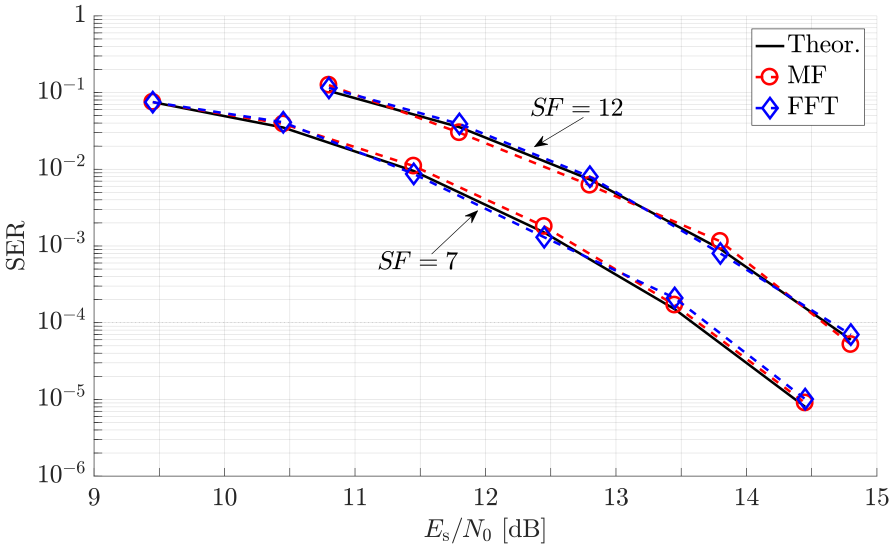

Figure 4.6: SER for strategies (4.8) and (4.9).

exactly the same of any other orthogonal modulation scheme and reads [38]

$$P_s = 1 - \frac{1}{\sqrt{2\pi}} \int_{-\infty}^{+\infty} e^{-x^2/2} \left[1 - \mathrm{Q}\left(x + \sqrt{2\frac{E_s}{N_0}} \right) \right]^{M-1} dx \tag{4.10}$$

where $\mathrm{Q}(\cdot)$ is the Gaussian Q function.

As said, strategies (4.8) and (4.9) are only approximately equivalent. In fact, strategy (4.9) has been obtained under the approximated assumption that LoRa signal (4.1) has a limited bandwidth $B/2$. Since this is not strictly true, it is interesting to evaluate the performance loss related to this approximation. In Figure 4.6 we report the symbol error rate (SER) versus E_s/N_0 of both strategies in the case of an uncoded transmission. For strategy (4.9) we also report the theoretical curve (4.10). The cases of $SF = 7$ and $SF = 12$ have been considered. It may be observed that both strategies have practically the same performance. We can conclude that the approximation that allows to obtain strategy (4.9) is very good.

4.3 Noncoherent Detection

Detection strategies (4.8) and (4.9) have been obtained under the assumption of ideal synchronization. We will now consider phase noise and the related performance loss it produces on strategies (4.8) and (4.9).

The optimal detection strategy in the presence of phase noise will depend on the channel coherence time. When the channel coherence time is long enough, we can exploit its correlation to design a receiver with memory with a negligible performance loss with respect to the case of ideal synchronization [39]. On the other end, when the channel phase is assumed to change independently every symbol interval, the system is again memoryless and the receiver will have the lowest possible complexity. It can be easily shown that when the channel phase is assumed uniformly distributed and to change independently every symbol interval, the strategies (4.8) and (4.9) become

$$\hat{a}_0 = \operatorname*{argmax}_{a_0} \left| z(a_0) \right| \tag{4.11}$$

and

$$\hat{a}_0 = \operatorname*{argmax}_{a_0} \left| \sum_{n=0}^{M-1} y_n e^{-j\frac{2\pi}{M}a_0 n} \right| . \tag{4.12}$$

These kinds of strategies are called "noncoherent" in the literature. In particular, we will consider strategy (4.12) only, since it can be implemented through the FFT.

Figure 4.7 reports, for $SF = 7$ and $SF = 12$, the SER performance of strategy (4.9) under the assumption of perfect knowledge of the channel phase, curves labeled "coherent", and that of strategy (4.12) under the assumption that the channel phase is unknown, constant over a symbol interval, and changing independently every symbol interval. It can be observed that the performance loss of this noncoherent strategy is lower than 0.5 dB. Thus, we believe that it is not worth investigating the possibility to exploit the phase noise correlation in case of a longer coherence time.

4.4 LoRaWAN Network Protocol

LoRaWAN networks typically are laid out in a star-of-stars topology in which gateways relay messages between IoT terminals and a central network server at the back-

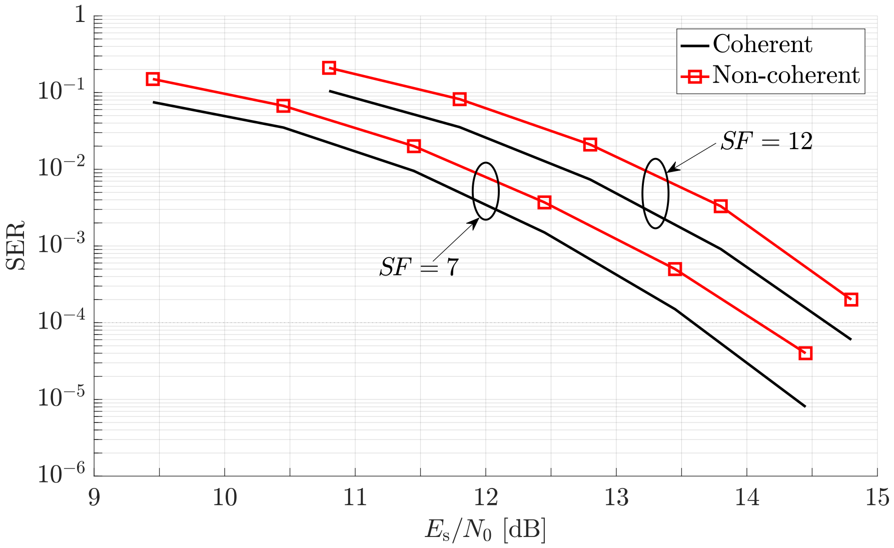

Figure 4.7: SER comparison between strategies (4.9) and (4.12).

end. Gateways are connected to the network server via standard Internet protocol connections while each client terminal (CT) use single-hop different modulation formats to one or many gateways. All links are generally bi-directional, although uplink communication from a CT to the network server is expected to be the predominant traffic.

Communication between CTs and gateways is spread out on different frequency channels and data rates. The LoRa network infrastructure can manage modulation format, data rate, and radio frequency output for each CT individually by means of an adaptive data rate scheme. The transmission parameters vary according to the considered geographical region and they must be compliant to those defined in the LoRaWAN standard.

The employed modulation formats are the LoRa and the Gaussian frequency shift keying (GFSK) modulation. Since the GFSK is used when the device is in close proximity to the gateway only, we can ignore it for satellite reception. Similarly, the mechanism by which different data rates are chosen will tend to push the CTs that have to send their messages to the cubesat to employ low data rates, i.e., high values

Region	**Bandwith [kHz]**	**SF**	**Data rate [bps]**	r_c
Europe, China	125	12	250	$4/6$
		11	440	
Europe, China, USA, Australia		10	980	$4/5$
		9	1760	
		8	3125	
		7	5470	
Europe, China	250	7	11000	$4/5$
USA, Australlia	500	12	980	$4/6$
		11	1760	
		10	3900	$4/5$
		9	7000	
		8	12500	
		7	21900	

Table 4.2: Data rates allowed by LoRaWAN for the LoRa signals.

of the SF. Thus, it is likely that the nanosat receiver will detect signals characterized by high SF values since they will be the only ones received with enough power to ensure error-free detection.

The selection of the transmission speed is a trade-off between communication range and message duration, and LoRaWAN data rates range from 0.25 kbps to 50 kbps, as shown in Table 4.2. We inferred the possible employed values of the code rate r_c simply inverting the formula for the bit rate $r_b = r_c SF \frac{B}{2^{SF}}$. From the found values, it results that the channel codes employed in LoRaWAN standard are not able to correct errors, but only to detect them.

The LoRaWAN standard specifies the radiated power either in terms of equivalent isotropic radiated antenna (EIRP) or in terms of equivalent radiated antenna (ERP) based on geographical region, as shown in Tab. 4.3. The difference between them

Region	**Radiated Power [dBm]**	**Measurement of the radiated power density**
Australia	10, 12, 14, 16, 18, 20, 22, 24, 26, **28**, **30**	EIRP
China	$-5, -2, 1, 4, 7, 10$	ERP
Europe	2, 5, 8, 11, 14, **20**	ERP
USA	10, 12, 14, 16, 18, 20, 22, 24, 26, **28**, **30**	EIRP

Table 4.3: Table of the possible value of radiated power density by LoRa terminal. In bold the values reserved exclusively to gateways.

is that for ERP, the antenna gain is expressed with reference to an ideal half-wave dipole antenna whereas, for EIRP, with reference to an ideal (theoretical) isotropic antenna. The relationship between ERP and EIRP is the following

$$\mathrm{EIRP}\Big|_{\mathrm{dBi}} = \mathrm{ERP}\Big|_{\mathrm{dBd}} + 10\log_{10} 1.64 = \mathrm{ERP}\Big|_{\mathrm{dBd}} + 2.15$$

where 1.64 is the gain of an ideal half-wave dipole antenna and the radiated power measurements expressed in dBi and dBd refer to an isotropic radiator and a dipole antenna, respectively.

CTs may transmit on any channel available at any time, using any available data rate, as long as the following rules are fulfilled:

- The CT changes channel in a pseudo-random fashion for every transmission. The resulting frequency diversity makes the system more robust to interferences.
- The CT does not exceed the maximum transmit *duty cycle* related to the used sub-band and local regulations.
- The CT does not exceed the maximum transmit duration (or *dwell time*) related to the used sub-band and local regulations.

The availale channels can be freely employed by the CTs. However, it is mandatory that every end-device will be able to employ at least some default channels and data

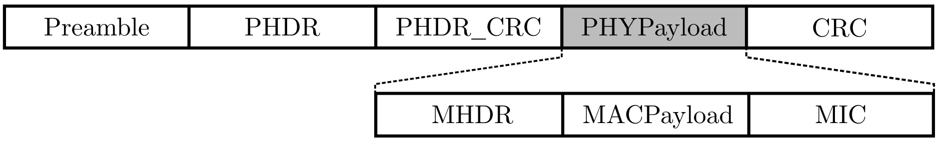

Figure 4.8: Radio physical layer structure of an uplink message.

rates. Some guard intervals are foreseen by the protocol. Regarding the case of signals with bandwidth $B = 125$ kHz, we know that they are transmitted employing a bandwidth of 200 kHz, whereas signals with $B = 500$ kHz are transmitted employing a bandwidth of 600 kHz. No information in the technical documents has been found related to the case of signals with bandwidth $B = 250$ kHz. In some regions, it is even possible to have the overlapped transmission of signals having different values of B so, as an example, a signal with $B = 500$ kHz will interfere with $3 \div 4$ signals having $B = 125$ kHz. We will see later that, taking into account the frequency instability of the employed oscillators and Doppler shift, we can have an uncompensated frequency offset of ± 50 kHz. Hence in the case of signals with $B = 125$ kHz, a guard interval of 75 kHz is not sufficient to avoid interference between two signals occupying two adjacent bandwidths.

CTs are allowed for bi-directional communications whereby each CT's uplink transmission is followed by two short downlink receive windows. The transmission slot scheduled by the CT is based on its own communication needs with a small variation based on a random time basis (ALOHA-type protocol). This operation is tailored for low power end-devices and applications that require downlink communication from the server only shortly after the CT has sent an uplink transmission. Downlink communications from the server at any other time will have to wait until the next scheduled uplink.

Uplink messages are sent by CTs to the network server relayed by one or many gateways. Their structure is shown in Figure 4.8. The preamble depends on the employed modulation format. In case of LoRa signals, the preamble is composed of 8 base up-chirps followed by 2 shifted up-chirps, whose shift in frequency is specific for LoRaWAN, and 2.25 conjugated base up-chirps (the so-called down-chirps). This

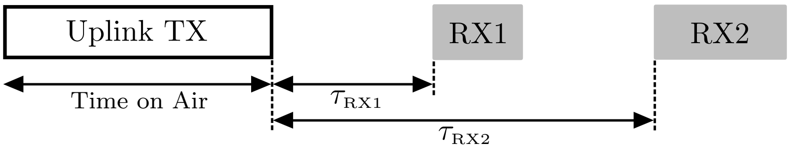

Figure 4.9: CT receive slot timing.

preamble should make easier to detect the beginning of a packet. The integrity of the payload `PHYPayload` is protected by another `CRC`. `PHDR` is an optional physical header protected by its own cyclic redundancy check (CRC), called `PHDR_CRC`. The `PHDR`, `PHDR_CRC`, and payload `CRC` fields are inserted by the radio transceiver. The field `PHYPayload` starts with a single-octet media access control (MAC) header `MHDR`, followed by a MAC payload `MACPayload` and ending with a 4-octet message integrity control.

As already mentioned, following each uplink transmission, the end-device opens two short receive windows. The receive window start times are defined using the end of the transmission as a reference (see Figure 4.9). The transmissions in the two receive windows employ a frequency and a data rate which are a function of the frequency and data rate used for the uplink and are also region-specific. An end-device will not transmit another uplink message before it either has received a downlink message in the first or second receive window of the previous transmission, or the second receive window of the previous transmission is expired.

4.5 System Simulator

We consider a scenario in which CTs are outside the coverage of terrestrial BTSs, its messages can be received by a cubesat, which orbit at 650 km, and transmitted back to the terrestrial radio access network. At the satellite, two options can be considered. In fact, detection can either be performed on board of the satellite or the received signal can be forwarded to be detected on ground. In both cases, assuming that the link from the cubesat to ground can be considered as error free, to the purpose of this feasibility study it is irrelevant if the receiver is located on board or on ground—the

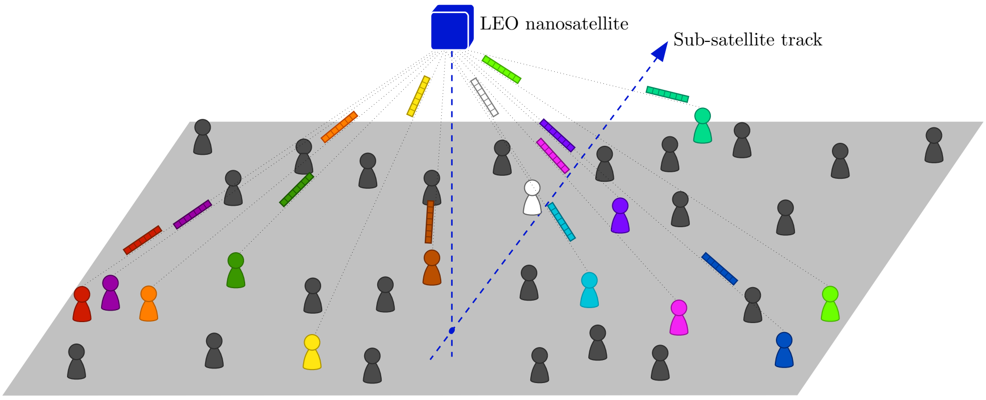

Figure 4.10: A graphical representation of the cubesat FoV.

choice on where to place the receiver depending on the overall complexity constraints on board of the cubesat.

The simulator operates in the time domain and it is based on the repetition of the following transmit-receive events. A network, in which a given number of users transmit packets to the cubesat following the LoRaWAN standard, is simulated. The cubesat is able to receive packets from different swaths within the entire field of view (FoV), as shown in Fig. 4.10.

We consider the receiver designed in [40]. The receiver tries to detect as many transmitted messages as possible, through successive detection and cancellation, and computes the number of correctly detected messages. The aim of the simulator is to derive

- the percentage of correctly received packets per SF and in total,
- the percentage of users whose transmitted packet is correctly decoded in at least one of the retransmissions (which can happen with different values of SF),

for a given users' density in the considered swaths.

4.5.1 Transmission Parameters

We assume that N_u active users are uniformly distributed within the FoV and that each CT transmits at the maximum allowed value of EIRP, which depends on the region of interest (see Section 4.4). Moreover, the data rate values also depend on the considered region and on the SF chosen for the packet transmission. Since the swaths can be huge, different areas (rural, urban, etc.) can be uniformly present in the FoV. CTs are classified into five classes, depending on the IoT application, and for each class a fraction of the distribution of all transmission parameters is specified. In other words, for the i-th application, a certain parameters' configuration (SF, length of payload, duty-cycle, etc.) that follows the input distribution, is associated to N_u^i active users, independently of their position.

Let us consider a given observation time T_o (sufficiently longer than the maximum length of a message in order to properly model the interference of different messages not perfectly overlapped in time). According to the number of messages transmitted by every terminal per day belonging to the i-th IoT class N_{msg}^i, the dimensions of the considered swath, and the density of users in a given frequency band (and in the adjacent bands), the number of transmitted packets is defined as follows

$$N_p = \frac{T_o}{3600 \cdot 24} \sum_i N_{\mathrm{msg}}^i N_u^i \, (1 + N_r),$$

where N_r is the number of successive retransmissions of a given packet. The cubesat will receive a fraction of these N_p packets.

4.5.2 Channel Model

Let N_p be the number of transmitted packets on a given frequency band and on a given swath. These packets are assumed to come from users uniformly distributed within the FoV (note that in case of $N_r = 0$ the association packet-user is univocal). Due to the random access, there is a probability that packets of two or more users collide. The model for the complex envelope of the received signal at the LEO satellite is thus

$$r(t) = e^{j\vartheta(t)} \sum_{i=1}^{N_p} \gamma_i(t) s_i(t - \tau_i) \exp\left\{ 2\pi\nu_i t + 2\pi t \int_0^t \nu_i' d\tau + \phi_i(t) \right\} + w(t)$$

where

- $s_i(t-\tau_i)$ is the i-th transmitted message.
  LoRa modulation has a complex envelope and a continuous phase. As a consequence, there is no need to take into account the non-linear distortions of the transmit amplifier,

- $\gamma_i(t)$ is its gain/attenuation introduced by the channel.
  The bandwidth of the transmitted signals is at most 500 kHz (more frequently 125 kHz), thus the channel results to be frequency flat. On a fading channel, this coefficient is complex and possibly time-varying. Since the main reason of time selectivity is related to the satellite speed, we neglect the very limited impact of the CT mobility and assume the channel to be static apart from the presence of the uncompensated frequency offset, the Doppler rate (taken into account separately), and the phase noise. Coefficients $\{\gamma_i\}$ can be thus considered as time-invariant for the whole packet duration,

- ν_i is the uncompensated frequency offset of signal $s_i(t)$.
  It takes into account both the Doppler shift and the frequency instability of the transmit oscillator oscillator only (± 30 parts per million (ppm), which corresponds to, approximately, ± 30 kHz) since the satellite receive oscillator is assumed much more stable.

- ν_i' is the Doppler rate,

- $\vartheta(t)$ is the receive phase noise,

- $\phi_i(t)$ is the phase noise at the i-th transmitter, assumed indipendent of the receive phase noise,

- τ_i is the relative delay of the i-th packet,

- $w(t)$ is the AWGN.

4.5.3 Complex Attenuation

Coefficients $\{\gamma_i\}$ take into account the radiation patterns of the employed antennas, the path losses, and other channel propagation effects. Since the antenna gain depends on the elevation angle and the receive power depends on the distance between the antenna feedpoints, these gains are influenced by the users positions. Moreover, different path loss models are taken into account depending on the environment where the CTs stand. For signals coming from rural areas, we believe that free-space path attenuation could be a good model, on the contrary the signal propagation attenuation in urban areas is modelled as a function of the m-th power of the distance between antennas.

We also include the fading effects. Considering that minimum elevation angle is not small, that the bandwidth of the transmitted signals is small and thus the channel results to be frequency flat, that we are interested in the rural areas where the CT concentration is lower, a Ricean fading model seems to be appropriate. However, we also take into account the presence of CTs in urban areas that can experience shadowing. Given the low values of transmitting power, the probability that a signal transmitted by one of such terminals can be received by the Cubesat is very low. We thus model the shadowing phenomen as a Bernoulli random variable with probability p, which reduces the user density by a factor p. Miscellaneous losses are also taken into account, to allow a conservative link budget design. In particular, we considered

- a 3 dB polarization mismatch,
- a 0.3 dB atmospheric loss due to rain, cloud, or oxygen absorption since the frequency bands defined in LoRaWAN protocol are within the sub-GHz spectrum [41,42].

4.5.4 Doppler Shift and Doppler Rate

For a given relative position of the satellite and the CT, the corresponding Doppler impairments are computed by using the approximations of circular satellite trajectory and constant satellite speed v_{sat}.

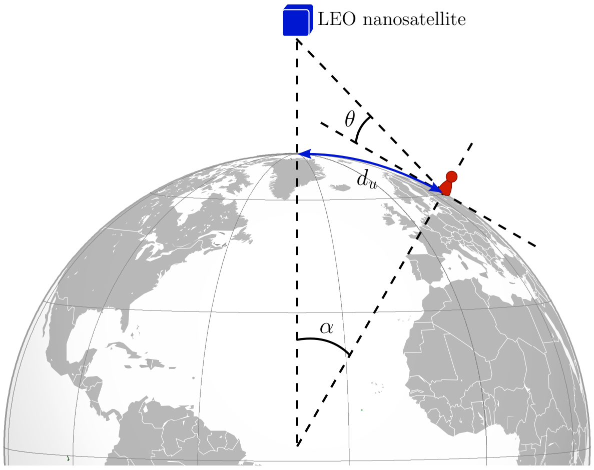

Figure 4.11: Graphical representation of the elevation angle θ and the distance d_u.

Let (x_u, y_u) be the position of the u-th user at time t on a spherical surface plane, with origin of the coordinate system (x, y) in the sub-satellite point on Earth and y axis towards the direction of motion of the satellite. The distance on this surface of the user from the origin can be cmputed through an extension of Pythagorean theorem on spherical surfaces

$$d_u(x_u, y_u) = R_\mathrm{E} \cos^{-1}\left(\cos\left(\frac{|x_u|}{R_\mathrm{E}}\right)\cos\left(\frac{|y_u|}{R_\mathrm{E}}\right)\right),$$

where R_E is the Earth radius. We define θ as the elevation angle of the satellite and it is possible to demonstrate what follows

$$\theta\left(x_u, y_u\right) = \frac{\pi}{2} - \tan^{-1}\frac{\sin\alpha\left(x_u, y_u\right)}{\frac{d}{R_\mathrm{E}} - \cos\alpha\left(x_u, y_u\right)} - \alpha\left(x_u, y_u\right)$$

where d is the satellite distance from the Earth center, and α the angle, measured at the Earth center between the sub-satellite point and the user. This angle can be simply expresses as $\alpha\left(x_u, y_u\right) = \frac{d_u(x_u, y_u)}{R_\mathrm{E}}$ by definition of radian. Fig. 4.11 shows a graphical representation of the involved variables.

Now, we can compute θ_max, which is the maximum elevation angle θ for a given user. It is easy to understand that the maximum elevation angle occurs when the

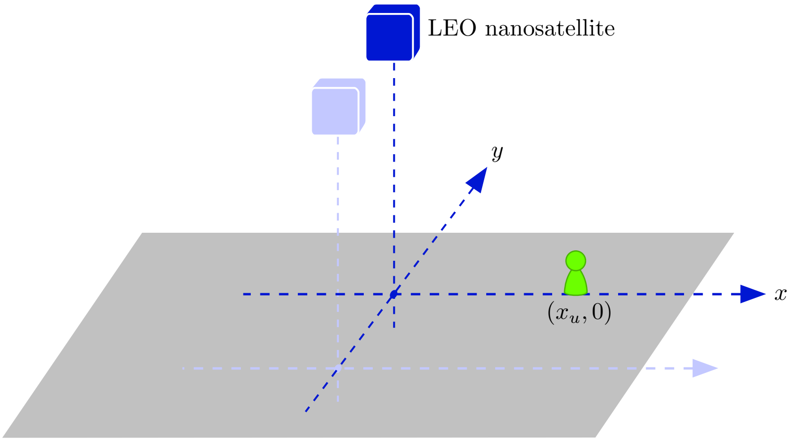

Figure 4.12: Graphical representation as seen from Nadir point: when the user sees the satellite at $\theta_{\max}$, he is in $(x_u, 0)$.

user and the sub-satellite point share the same y coordinate, i.e., when the user is in location with coordinates $(x_u, 0)$ (see Fig. 4.12). As a consequence $\theta_{\max} = \theta\,(x_u, 0)$.

Finally, calling c the speed of light and f_0 the frequency of the employed carrier, we can express the Doppler shift $\nu(t)$ at time t as [43]

$$\nu(t) = -\frac{f_0}{c}\frac{R_{\mathrm{E}} d \sin(\Delta\psi(t)) \cos\Big(\cos^{-1}\Big(\frac{R_{\mathrm{E}}}{d}\cos\theta_{\max}\Big) - \theta_{\max}\Big)\omega_{\mathrm{sat}}}{\sqrt{R_{\mathrm{E}}^2 + d^2 - 2R_{\mathrm{E}} d \cos(\Delta\psi(t)) \cos\Big(\cos^{-1}\Big(\frac{R_{\mathrm{E}}}{d}\cos\theta_{\max}\Big) - \theta_{\max}\Big)}}$$

where $\omega_{\mathrm{sat}} = \frac{v_{\mathrm{sat}}}{d}$ is the angular speed of the satellite and $\Delta\psi(t)$ the angle, measured at the Earth center, between the sub-satellite point at time t and the sub-satellite point at the instant the CT observes the satellite at the maximum elevation angle. The latter angle can be obtain as follows

$$\Delta\psi\,(t) = -\frac{y_u}{R_{\mathrm{E}}}\,.$$

The Doppler rate $\nu'(t)$ is the the first derivative of $\nu(t)$,

$$\nu'(t) = \frac{\mathrm{d}}{\mathrm{d}t}\nu(t),$$

that can be expressed as

$$\nu'(t) = -\frac{f_0}{c}\omega_{\mathrm{sat}}^2 \left[\frac{R_{\mathrm{E}} d \cos(\Delta\psi(t))\chi}{\sqrt{R_{\mathrm{E}}^2 + d^2 - 2R_{\mathrm{E}} d \cos(\Delta\psi(t))\,\chi}} \right.$$
$$\left. -\frac{1}{2}\frac{\big(R_{\mathrm{E}} d \sin(\Delta\psi(t))\chi\big)^2}{\sqrt[\frac{3}{2}]{R_{\mathrm{E}}^2 + d^2 - 2R_{\mathrm{E}} d \cos(\Delta\psi(t))\chi}} \right]$$

where $\chi = \cos\Big(\cos^{-1}\Big(\frac{R_{\mathrm{E}}}{d}\cos\theta_{\max}\Big) - \theta_{\max}\Big)$ and, clearly, $\frac{d}{dt}\Delta\psi\,(t) = \omega_{\mathrm{sat}}$. We can compute the maximum values of both the Doppler shift and the Doppler rate by substituting the coordinates of the points which experience the worst Doppler effect. Considering the horizon of the LEO satellite and the higher frequency carrier defined in LoRaWAN protocol,[2] the Doppler shift and the Doppler rate values result to be

$$|\nu(t)| \leq 21.15 \text{ kHz} \qquad \big|\nu'(t)\big| \leq 245 \text{ Hz/s}$$

Fig. 4.13 shows the Doppler profile for the above-mentioned scenario.

4.5.5 Antenna Patterns

We assume that the CT is equipped with a quarter-wave monopole, one of the most employed low-cost antennas used in IoT applications thanks to its omnidirectionality. The radiation pattern of the monopole is given by

$$F(\theta) = \frac{\cos\big(\frac{\pi}{2}\cos\left(\frac{\pi}{2} - \theta\right)\big)}{\sin\big(\frac{\pi}{2} - \theta\big)}$$

where θ is the elevation angle [45]. This antenna has a null in the azimuthal direction, as shown in Fig. 4.14.

At the receiver side, we assume that the cubesat is equipped with helical antennas. This kind of antenna is widely used in nanosatellite applications thanks to its

---

[2] The worst case refers to a signals transmission in Australia using the 928 MHz channel [44].

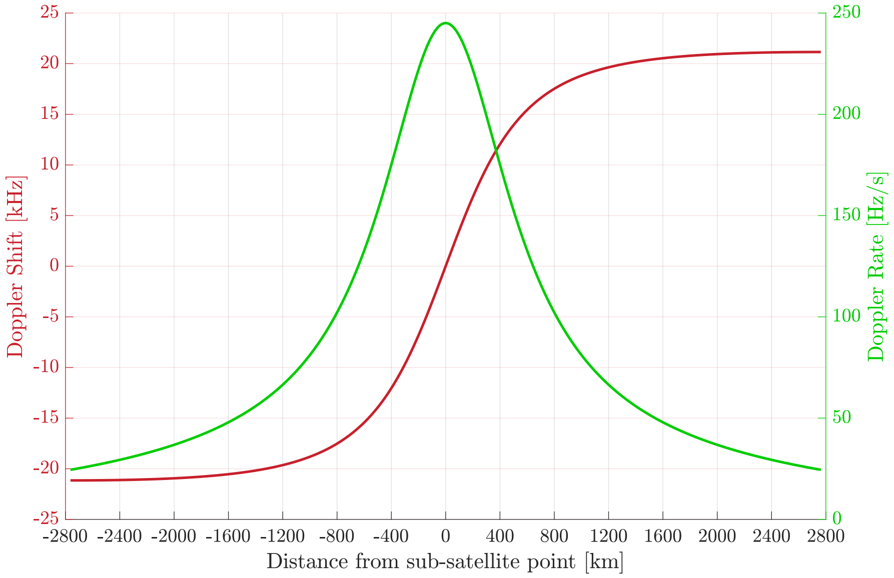

Figure 4.13: Doppler shift and Doppler rate values for a LEO satellite flown over the Australian region.

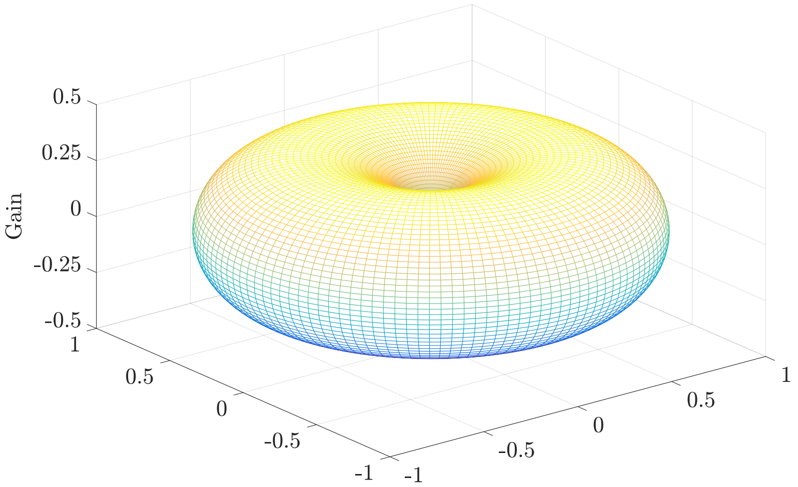

Figure 4.14: Radiation pattern of a $\lambda/4$ dipole.

wide bandwidth, the ease of realization and the reduced size [46–48]. The theoretical antenna pattern is

$$F(\theta) = \frac{\pi}{2}\cos\theta\,\frac{\sin\left(\frac{\pi}{\lambda}NS(\cos\theta - 1) - \frac{\pi}{2}\right)}{\frac{\pi}{\lambda}NS(\cos\theta - 1) - \frac{\pi}{2}}$$

where θ is the elevation angle, λ is the wavelength, N the number of turns, and S the spacing between turns, while the antenna gain can be computed using the approximation

$$G = 6.2N\frac{S}{\lambda}\left(\frac{\pi D}{\lambda}\right)^2 \text{ [dB]}$$

where D is the diameter of the helix [45].

Considered the regional parameters specified in [44], a cubesat operating in an European scenario must be able to receive signal with wavelenght in the range $34.4 \div 34.7$ centimeters. Since a common helix antenna design rule uses $S = \lambda/4$, we set $S = 8.63$ centimeters and, adopting $N = 8$ and $D = 10.5$ centimeters, the gain results $G = 12.39$ dB. Fig. 4.15 shows the normalized radiation pattern for the 8-turn helical antenna above-mentioned.

As the antenna gain pattern is assumed to be axially symmetric, the gain is only dependent on the elevation angle from the antenna and all antennas pointing at 55 degrees from Nadir perpendicular to the direction of travel in order to optimize the coverage.

4.5.6 Link Budget

Let P_{TX} be the power transmitted by the user terminal, that depends on the considered region [44], L the free-space path loss, G_{TX} the transmitter antenna gain, G_{RX} the receiver antenna gain, $k_B = 1.38064852 \cdot 10^{-23}$ J/K the Boltzmann constant, $T_N = 450$ K the equivalent noise temperature and L_M the miscellaneous losses. The carrier-to-noise ratio (CNR) seen by the satellite can be written by using the Friis trasmission equation

$$\left.\frac{C}{N}\right|_{\mathrm{dB}} = \left.P_{\mathrm{TX}}\right|_{\mathrm{dBm}} + \left.L\right|_{\mathrm{dB}} + \left.G_{\mathrm{TX}}\right|_{\mathrm{dB}} + \left.G_{\mathrm{RX}}\right|_{\mathrm{dB}} - 10\log_{10}(k_B T_N) + \left.L_M\right|_{\mathrm{dB}},$$

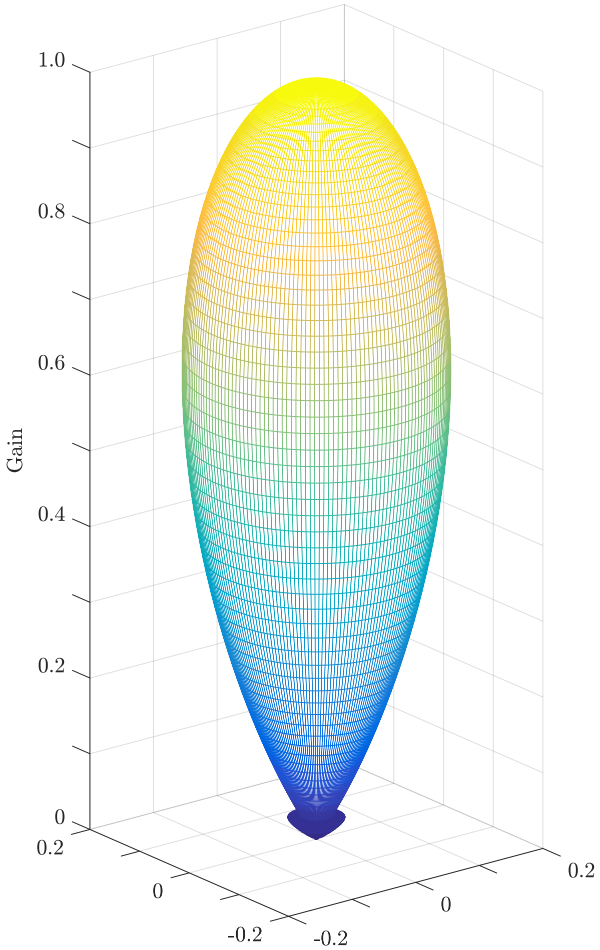

Figure 4.15: Normalized radiation pattern of a 8-turns helical antennas.

where C is the received modulated carrier signal power and N the noise power after the receiver filters. The attenuation due to the propagation in free-space can be computed as follows

$$L\Big|_{\text{dB}} = 20\log_{10}\left(\frac{\lambda}{2\pi}\right) - 20\log_{10}(R_u)$$

where R_u is the distance between the user and the satellite, according to the user's position in the FoV. It is easy to verify by the rule of cosine that

$$R_u = \sqrt{d^2 + R_{\text{E}}^2 - 2R_{\text{E}}d\cos\alpha(x_u, y_u)}.$$

The gain G_{TX} depends on the position of the user by the angle $\theta(x_u, y_u)$, as explained in Sec. 4.5.5. Thanks to the symmetries of the receiving antenna, G_{RX} depends only on the angular distance ϕ between the center of the beam (i.e., the direction of maximum of its pattern) and the user. This can be computed by the law of cosine as

$$\phi = \cos^{-1}\left(\frac{d_{u,\max}^2 - R_u^2 - R_{\max}^2}{2R_u R_{\max}}\right),$$

where $R_{\max}$ is the distance between satellite and maximum illumination point and $d_{u,\max}$ the linear distance between the user and the maximum illumination point. These distances and angles are shown in Fig. 4.16. Denoting by θ_{tilt} the inclination angle of the satellite antenna measured from the Zenith, we can obtain $d_{u,\max}$ as

$$d_{u,\max} = 2R_{\text{E}}\tan^{-1}\left(\frac{\left(1 - \sqrt{1 + \tan\theta_{\text{tilt}} - \frac{d^2}{R_{\text{E}}^2}\tan^2\theta_{\text{tilt}}}\right)}{\left(1 + \frac{d}{R_{\text{E}}}\right)\tan\theta_{\text{tilt}}}\right)$$

and $R_{\max}$ in a way similar to R_u through the following equation

$$R_{\max} = \sqrt{d^2 + R_{\text{E}}^2 - 2R_{\text{E}}d\cos\left(\frac{d_{u,\max}}{R_{\text{E}}}\right)}.$$

Once the CNR is known, it is possible to compute, respectively, the ratios between the mean energy per bit and per symbol over the noise PSD E_s/N_0 and E_b/N_0 as

$$\frac{E_s}{N_0}\Big|_{\text{dB}} = \frac{C}{N}\Big|_{\text{dB}} + 10\log_{10}(2^{SF})$$

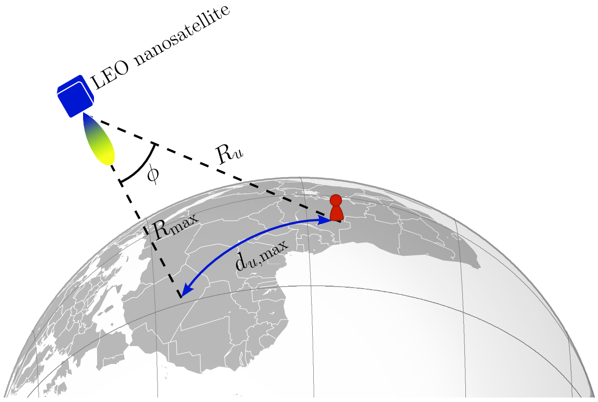

Figure 4.16: Representation of the distances and angles mentioned in the derivation of the link budget.

$$\begin{aligned} \left.\frac{E_b}{N_0}\right|_{\text{dB}} &= \left.\frac{C}{N}\right|_{\text{dB}} + 10\log_{10}\left(\frac{2^{SF}}{SF}\right) - 10\log_{10} r_c \\ &= \left.\frac{E_s}{N_0}\right|_{\text{dB}} - 10\log_{10}(SF) - 10\log_{10} r_c \end{aligned} \tag{4.13}$$

where r_c is the forward error correction (FEC) code rate.

Fig. 4.17 shows the link budget for the European scenario when all terminals are transmitting at the maximum allowed EIRP over the 866.3 MHz channel, the cubesat is equipped with a 8-turns antenna, and $L_M = 3.3$ dB.

Let us now make some considerations on the closure of the link budget. A LoRa signal with a given value of SF is perfectly equivalent, in terms of performance over the AWGN channel, to an M-ary frequency shift keying (FSK) modulation with $M = 2^{SF}$ (see Sec. 4.2). For M-FSK signals over the AWGN channel there is a closed-form expression of the BER versus E_b/N_0

$$P_b \approx 2^{SF-1}\,\mathrm{Q}\left(\sqrt{\frac{E_b}{N_0}SF}\right),$$

where $\mathrm{Q}(\cdot)$ is the Gaussian Q-function. Considering that E_b/N_0 is related to the CNR, as seen in (4.13), for a BER of 10^{-5} the corresponding CNR values are shown

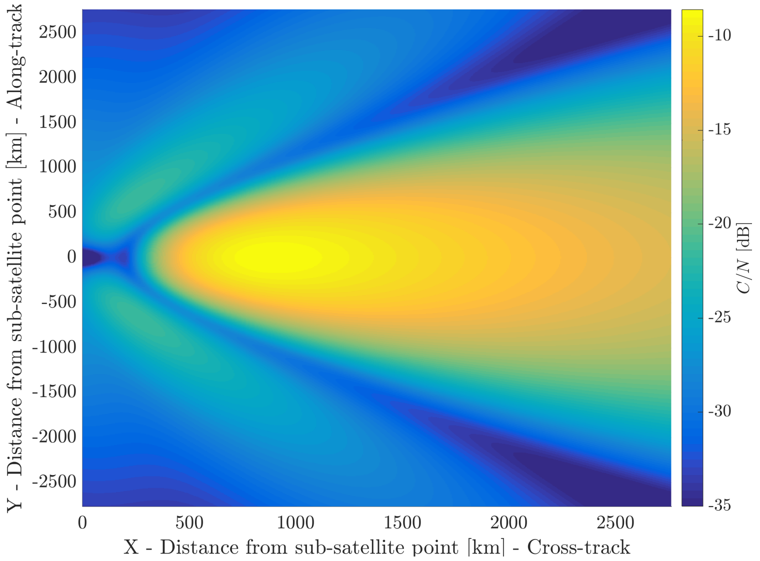

Figure 4.17: Spatial distribution of C/N on the entire horizon for the European scenario when the receiving antenna is a 8-turns helical antenna.

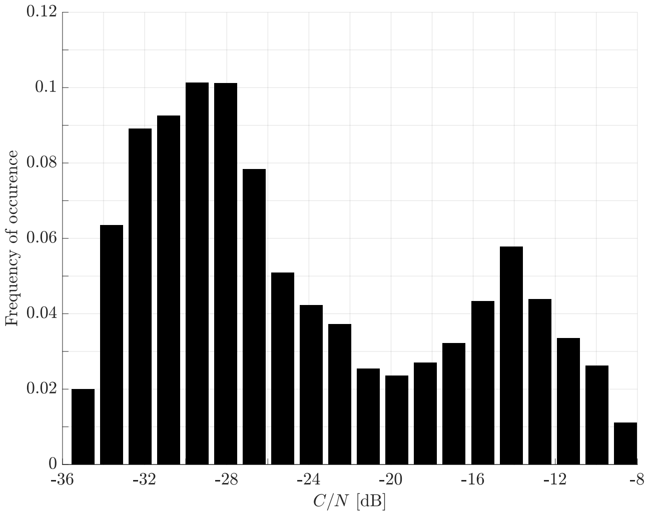

Figure 4.18: Probability distribution of C/N on the entire horizon for the European scenario when the receiving antenna is a 8-turns helical antenna.

SF	C/N **[dBW]**	**SF**	C/N **[dBW]**
7	-6.9	10	-15.3
8	-9.7	11	-18.1
9	-12.5	12	-20.9

Table 4.4: CNR values required to achieve a BER $= 10^{-5}$ over AWGN channel, uncoded transmission and no interfering signals.

in Tab. 4.4. Comparing these results with those shown in Fig. 4.18, it can be concluded that not all values of the SF can achieve the target BER. Moreover, it has to be considered that our scenario is **interference limited and not AWGN limited**, so the set of available parameters will be further restricted. Reasonably, it is expected that the most decoded signals are LoRa signals with high values of SF.

4.5.7 Phase Noise

We expect that the CTs employ very cheap oscillators whereas we may assume that the oscillator at the satellite has much better characteristics. For this reason, we only consider the transmit phase noise.

The phase noise process can be modeled according to the interpolated version of the PSD mask reported in a datasheet of a commercial LoRa transceiver datasheet [49] and its PSD is shown in Fig. 4.19. In the continuous-time domain, it could be generated by filtering a white noise process with a filter whose frequency response $H(f)$ is such that $|H(f)|^2$ approximates the target mask. A single-pole transfer function of the form

$$H(s) = k\left(1 + \frac{s}{p}\right)^{-1}$$

with $\frac{p}{2\pi} = 100$ kHz and $k = 10^{-5.15}$, is such that we obtain a very good approximation of the considered mask, as shown in Fig 4.19.

To implement it in discrete time domain, we could use the bilinear transform $s = \frac{2}{T_c}\frac{z-1}{z+1}$, where T_c is the sampling interval, with prewarping to obtain the transfer

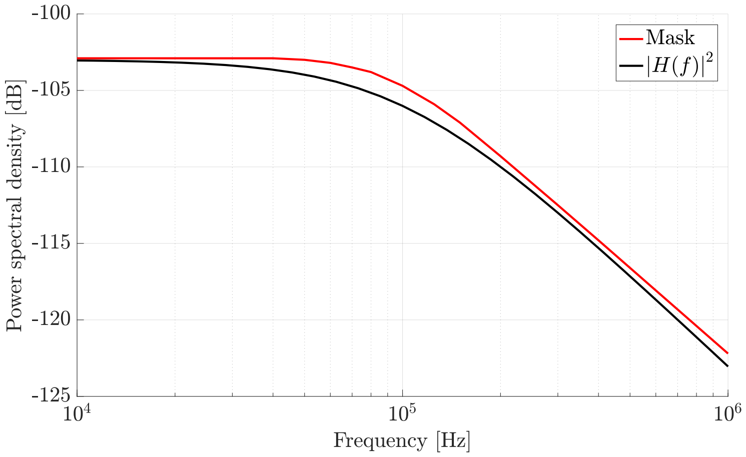

Figure 4.19: PSD of the phase noise compared to the implemented frequency response.

function $H(z)$ in the z domain [50]. The resulting filter is

$$H(z) = k\frac{T_c p'}{T_c p' + 2}\frac{1+z^{-1}}{1+\frac{z^{-1}}{(T_c p'+2)/(T_c p'-2)}}$$

where $p' = \frac{2}{T_c}\tan\left(\frac{pT_c}{2}\right)$. It can be implemented through a simple infinite impulse response filter.

Although this model well describes the realistic hardware behaviour, we decided to implement a more challenging phase noise based on the Wiener model. The advantage of this model is that it depends on a single parameter which can be used to tune its strength.

4.6 Receiver Performance

Finally we present the performance of the receiver designed in [40], working in a realistic operative scenario. The following results refer to an European scenario in which each CT works according to the LoRaWAN standard, transmitting 12-byte packets with bandwidth $B = 125$ kHz at 14 dB EIRP on the 866.3 MHz channel. For

SF	Probability	SF	Probability
7	0	10	$\frac{4}{31}$
8	$\frac{16}{31}$	11	$\frac{2}{31}$
9	$\frac{8}{31}$	12	$\frac{1}{31}$

Table 4.5: Probability distribution of the SF values in the scenario under study.

simplicity, we consider only one class of IoT terminals, not enabled to the packets retransmission, whose distribution of SF values is described in Tab. 4.5. No interfering signals with bandwidth $B = 500$ kHz and no co-channel interferences are taken into account. Though the interference arising from the packet transmissions occured in the entire FoV, the performance analysis will be restricted to a well defined geographical area and all results will be as a function of the number of transmitted packets within the swath.

The spatial distribution of the detected packets within the entire FoV and the swath under study having size 678×544 km are shown in Fig. 4.20. As predicted in Sec. 4.5.6, from the link budget point of view, LoRa signals with high values of SF are easier detectable, despite they are received in geographical areas illuminated by the antenna sidelobes. However, their detection is problematic due to the higher sensitivity to the Doppler effect. Packets with $SF = 8$ and $SF = 9$ can be instead received only in a region in which the gain of the satellite antenna is maximum. For the sake of completeness, Fig. 4.21 depicts the probability distribution E_s/N_0 for the transmitted packets in the entire FoV, highlighting the statistics of packets detected within the swath.

Fig. 4.22 shows the percentage of successfully detected packets per SF from an ideal receiver which perfectly estimates and compensates the unknown channel parameters. The solid line refers to an interference cancellation (IC) scheme able to remove at least 90% of the amplitude of each successfully detected packet, whereas the dashed line refers to the case of absence of interference cancellation. The fast decrease of the probability of successful detection with lower SFs depends on the SF probability distribution itself— the higher the probability of packets transmitted

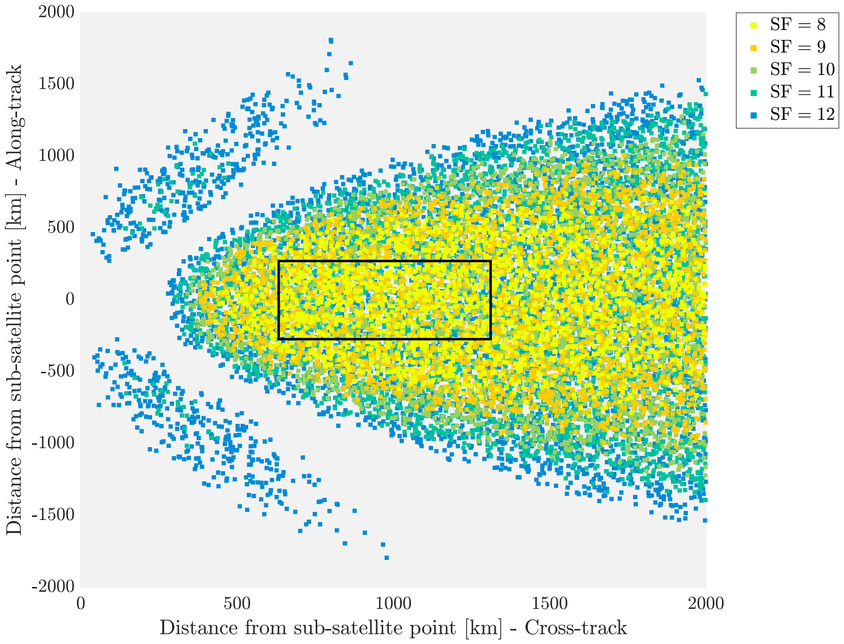

Figure 4.20: Spatial distribution of the detected packets in the satellite FoV. The borders of the considered swath are delimited in black.

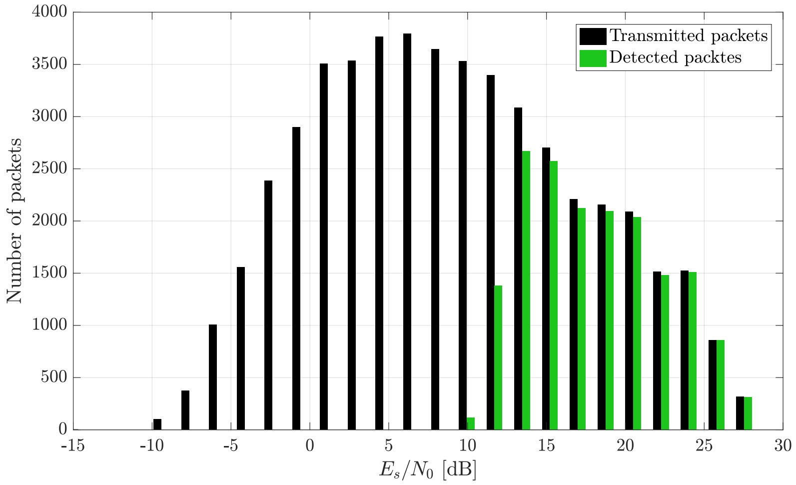

Figure 4.21: Probability distribution of E_s/N_0 in the entire FoV of the cubesat.

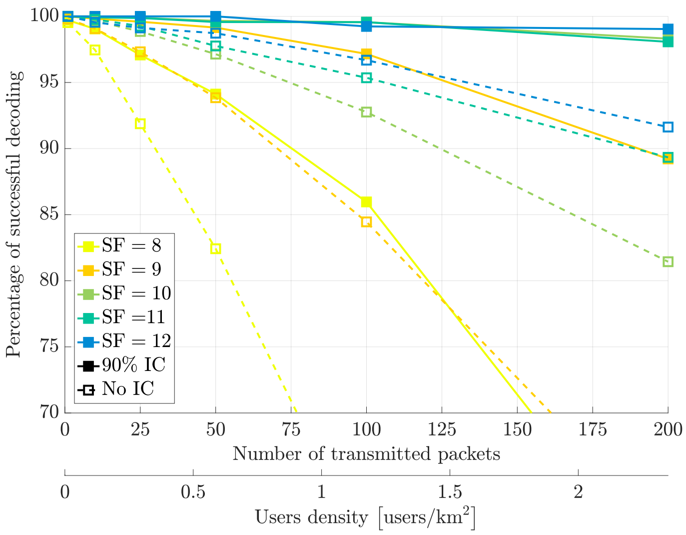

Figure 4.22: Percentage of successful decoding per SF for ideal impairments compensation.

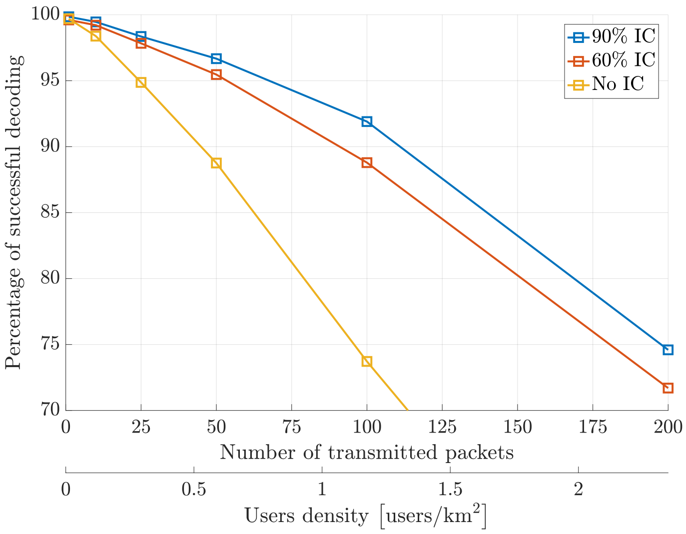

Figure 4.23: Mean percentage of successful decoding, averaged on all SFs, for ideal impairments compensation.

with a given SF value, the more frequently the collisions between packets with that SF value. Note that collisions between packets with different SF does not affect the performance thanks to their orthogonality, as explained in Sec. 4.1.

From the comparison shown in Fig. 4.23 between different amounts of rejection of the IC scheme, it results that a significant improvement can be obtained by allowing the receiver to remove the detected packets from the received signal. However, the cancellation does not need to be perfect. In fact, there is a limited loss between the cases when 60% and 90% of the amplitude of each successfully detected packet is removed. This proves that LoRa waveform is resilient to the effects of the imperfect signal cancellation and allows to relax the precision of the estimates computed by the IC algorithm, thus reducing the complexity.

The performance of the proposed receiver is illustrated in Figs. 4.24 and 4.25. These curves show how the proposed scheme is able to recover the unknown channel parameters, almost reaching the same performance as the ideal receiver which perfectly estimates and compensates the channel parameters and is also able to cancel at least 90% of the amplitude of each successfully detected packet, in case of few transmitting CTs.

To understand the robustness of the proposed receiver, in Fig. 4.25 we report the amount of traffic in the LoRaWAN network, expressed as the mean number of observed packets in a generic time instant in function of the number of transmitted packets. Even if the number of collisions increases quickly, due to the larger number of transmitting terminals, we can see that almost 75% of the transmitted packets can be decoded by the proposed receiving architecture, also when more than 40 collisions occur.

In view of this fact, we can conclude that the receiver for LoRa signals designed in [40] is able to cope with the main impairments related to a LEO satellite reception, such as Doppler shift and Doppler rate, and exploiting interference cancellation scheme, it is able to significantly improve the overall network performance. Since the receiver has a very high robustness to interference, thanks also to the intrinsic robustness of the modulation format, we can assert that it is reasonable to assume that this modulation format, with the designed receiver, is suitable for the satellite-based

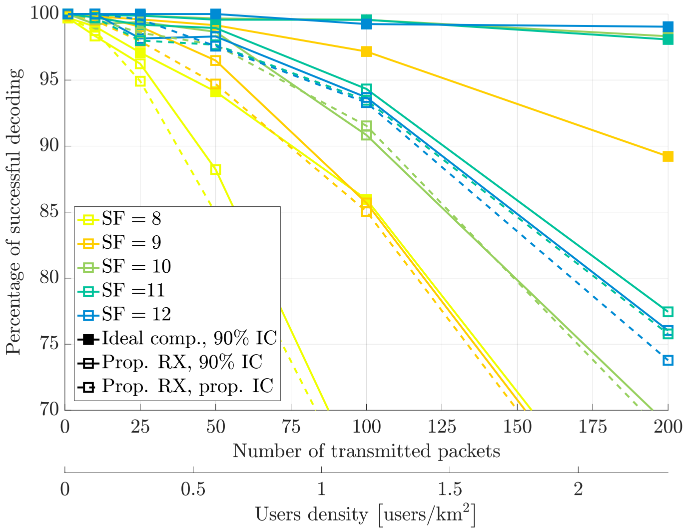

Figure 4.24: Comparison between the receivers in terms of mean percentage of successfully detected packets per SF.

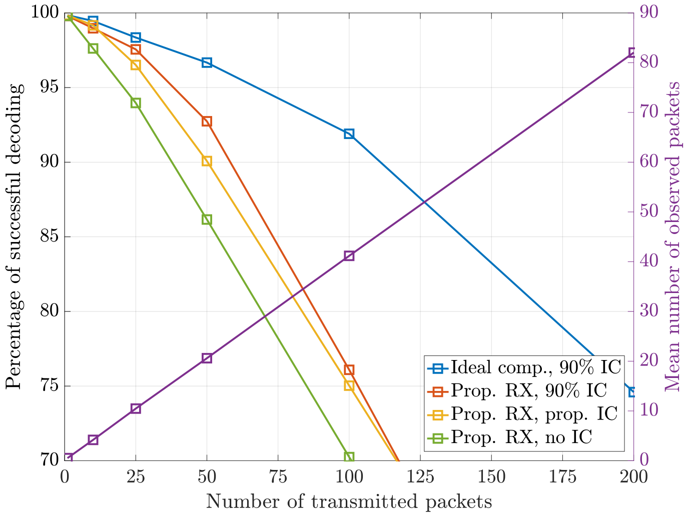

Figure 4.25: Comparison between different levels of amplitude interference reduction in terms of mean percentage of successfully detected packets, averaged on all SFs.

applications.

4.7 Conclusion

The problem of the coverage extension of IoT networks through the use of LEO satellites was considered. First, we have investigated the modulation aspects of the LoRa waveform and the issues concerning the signal detection by cubesats. We have implemented a LoRaWAN network simulator and the performance of the proposed receiver has been finally assessed.

Bibliography

[1] G. D. Forney, Jr., “Maximum-likelihood sequence estimation of digital sequences in the presence of intersymbol interference,” *IEEE Trans. Inform. Theory*, vol. 18, pp. 284–287, May 1972.

[2] G. Ungerboeck, “Adaptive maximum likelihood receiver for carrier-modulated data-transmission systems,” *IEEE Trans. Commun.*, vol. com-22, pp. 624–636, May 1974.

[3] P. Robertson, E. Villebrun, and P. Hoeher, “A comparison of optimal and suboptimal MAP decoding algorithms operating in the log domain,” in *Proc. IEEE Intern. Conf. Commun.*, (Seattle, WA), pp. 1009–1013, 1995.

[4] D. M. Arnold, H.-A. Loeliger, P. O. Vontobel, A. Kavčić, and W. Zeng, “Simulation-based computation of information rates for channels with memory,” *IEEE Trans. Inform. Theory*, vol. 52, pp. 3498–3508, Aug. 2006.

[5] N. Merhav, G. Kaplan, A. Lapidoth, and S. Shamai, “On information rates for mismatched decoders,” *IEEE Trans. Inform. Theory*, vol. 40, pp. 1953–1967, Nov. 1994.

[6] F. Rusek and J. B. Anderson, “The two dimensional Mazo limit,” in *Proc. IEEE International Symposium on Information Theory*, (Adelaide, Australia), pp. 970–974, Nov. 2005.

[7] A. Barbieri, D. Fertonani, and G. Colavolpe, “Time-frequency packing for linear modulations: spectral efficiency and practical detection schemes,” *IEEE Trans. Commun.*, vol. 57, pp. 2951–2959, Oct. 2009.

[8] ETSI EN 302 307-2 Digital Video Broadcasting (DVB), Second generation framing structure, channel coding and modulation systems for broadcasting, interactive services, news gathering and other broadband satellite applications, Part II: S2-Extensions (DVB-S2X). Available on ETSI web site (http://www.etsi.org).

[9] ETSI EN 300 421 Digital Video Broadcasting (DVB), Framing structure, channel coding and modulation for 11/12 GHz satellite services. Available on ETSI web site (http://www.etsi.org).

[10] ETSI EN 302 307-1 Digital Video Broadcasting (DVB), Second generation framing structure, channel coding and modulation systems for broadcasting, interactive services, news gathering and other broadband satellite applications, Part I: DVB-S2. Available on ETSI web site (http://www.etsi.org).

[11] S. Cioni, G. Colavolpe, V. Mignone, A. Modenini, A. Morello, M. Ricciulli, A. Ugolini, and Y. Zanettini, “Transmission parameters optimization and receiver architectures for DVB-S2X systems,” *International Journal of Satellite Communications and Networking*, vol. 34, pp. 337–350, May/June 2016. Article first published online: June 2015.

[12] A. Ugolini, A. Modenini, G. Colavolpe, V. Mignone, and A. Morello, “Advanced techniques for spectrally efficient DVB-S2X systems,” *International Journal of Satellite Communications and Networking*, vol. 34, pp. 609–623, Sep./Oct. 2016. Article first published online: September 2015.

[13] A. Barbieri and G. Colavolpe, “On pilot-symbol-assisted carrier synchronization for DVB-S2 systems,” *IEEE Trans. Broadcast.*, vol. 53, pp. 685–692, Sept. 2007.

[14] E. Casini, R. De Gaudenzi, and A. Ginesi, “DVB-S2 modem algorithms design and performance over typical satellite channels,” *International Journal of Satellite Communications and Networking*, vol. 22, pp. 281–318, 2004.

[15] D. Godard, “Self-recovering equalization and carrier tracking in two-dimensional data communication systems,” *IEEE Trans. Commun.*, vol. 28, pp. 1867–1875, Nov. 1980.

[16] A. Swami and B. M. Sadler, “Hierarchical digital modulation classification using cumulants,” *IEEE Trans. Commun.*, vol. 48, pp. 416–429, Mar. 2000.

[17] O. A. Dobre, Y. Bar-Ness, and W. Su, “Higher-order cyclic cumulants for high order modulation classification,” in *Military Communications Conference, 2003. MILCOM’03. 2003 IEEE*, vol. 1, pp. 112–117, IEEE, 2003.

[18] V. D. Orlic and M. L. Dukic, “Automatic modulation classification algorithm using higher-order cumulants under real-world channel conditions,” *IEEE Commun. Letters*, vol. 13, no. 12, 2009.

[19] P. Serena and A. Bononi, “A time-domain extended gaussian noise model,” *J. Lightwave Tech.*, vol. 33, pp. 1459–1472, Apr. 2015.

[20] O. A. Dobre, A. Abdi, Y. Bar-Ness, and W. Su, “Survey of automatic modulation classification techniques: classical approaches and new trend,” *IET Communications*, vol. 1, no. 2, pp. 137–156, 2007.

[21] G. Sun, “MPSK signals modulation classification using sixth-order cumulants,” in *3rd International Congress on Image and Signal Processing (CISP)*, vol. 9, pp. 4404–4407, 2010.

[22] R. Piazza, B. Shankar, E. Zenteno, D. Ronnow, J. Grotz, F. Zimmer, M. Grasslin, F. Heckmann, and S. Cioni, “Multicarrier digital pre-distortion/equalization techniques for non-linear satellite channels,” in *Proc. AIAA Intern. Communications Satellite Systems Conf.*, (Ottawa, Canada), Sept. 2012.

[23] R. Piazza, B. M. R. Shankar, and B. Ottersten, “Data predistortion for multicarrier satellite channels based on direct learning,” *IEEE Trans. Signal Processing*, vol. 62, pp. 5868–5880, Nov. 2014.

[24] B. Beidas, “Intermodulation distortion in multicarrier satellite systems: analysis and turbo volterra equalization,” *IEEE Trans. on Commun.*, vol. 59, pp. 1580–1590, June 2011.

[25] A. Ugolini, Y. Zanettini, A. Piemontese, A. Vanelli-Coralli, and G. Colavolpe, “Efficient satellite systems based on interference management and exploitation,” in *Proc. Asilomar Conf. Signals, Systems, Comp.*, Sept. 2016.

[26] H. Meyr, M. Oerder, and A. Polydoros, “On sampling rate, analog prefiltering, and sufficient statistics for digital receivers,” *IEEE Trans. Commun.*, vol. 42, pp. 3208–3214, Dec. 1994.

[27] A. Modenini, *Advanced transceivers for spectrally-efficient communications*. PhD thesis, University of Parma, Parma, Italy, Jan. 2014.

[28] U. Fincke and M. Pohst, “Improved methods for calculating vectors of short length in a lattice, including a complexity analysis,” *Mathematics of computation*, vol. 44, pp. 463–471, Apr. 1985.

[29] G. Colavolpe, G. Ferrari, and R. Raheli, “Reduced-state BCJR-type algorithms,” *IEEE J. Select. Areas Commun.*, vol. 19, pp. 848–859, May 2001.

[30] A. Modenini, F. Rusek, and G. Colavolpe, “Adaptive rate-maximizing channel-shortening for ISI channels,” *IEEE Commun. Letters*, vol. 19, pp. 2090–2093, Dec. 2015.

[31] L. R. Bahl, J. Cocke, F. Jelinek, and J. Raviv, “Optimal decoding of linear codes for minimizing symbol error rate,” *IEEE Trans. Inform. Theory*, vol. 20, pp. 284–287, Mar. 1974.

[32] S. Verdú, *Multiuser detection*. Cambridge, UK: Cambridge University Press, 1998.

[33] B. Beidas, R. Seshadri, and N. Becker, “Multicarrier successive predistortion for nonlinear satellite systems,” *IEEE Trans. on Commun.*, vol. 63, pp. 1373–1382, Apr. 2015.

[34] G. Karam and H. Sari, “Analysis of predistortion, equalization, and ISI cancellation techniques in digital radio systems with nonlinear transmit amplifiers,” *IEEE Trans. Commun.*, vol. 37, pp. 1245–1253, Dec 1989.

[35] N. Sornin and M. Luis and T. Eirich and T. Kramp and O. Hersent, LoRaWAN specification. Version 1.0.2. June 2016.

[36] S. G. Wilson, *Digital modulation and coding*. Prentice Hall, 1996.

[37] I. S. Gradshtein and I. M. Ryzhik, *Table of integrals, series and products*. New York: Academic Press, 1980.

[38] S. Benedetto and E. Biglieri, *Principles of digital transmission: with wireless applications*. Norwell, MA, USA: Kluwer Academic Publishers, 1999.

[39] G. Colavolpe and R. Raheli, “Theoretical analysis and performance limits of noncoherent sequence detection of coded PSK,” *IEEE Trans. Inform. Theory*, vol. 46, pp. 1483–1494, July 2000.

[40] M. Ricciulli, *Advanced transceivers for satellite communications*. PhD thesis, University of Parma, Parma, Italy, Oct. 2017.

[41] Recommendation ITU-R P.840-6, “Attenuation due to clouds and fog,” Geneve, 2013.

[42] Recommendation ITU-R P.530-16, “Propagation data and prediction methods required for the design of terrestrial line-of-sight systems,” Geneve, 2015.

[43] I. Ali, N. Al-Dhahir, and J. E. Hershey, “Doppler characterization for LEO satellites,” *IEEE Trans. Commun.*, vol. 46, pp. 309–313, Mar. 1998.

[44] LoRa Alliance, Inc, LoRaWAN regional specifications. June 2016.

[45] W. L. Stutzman and G. A. Thiele, eds., *Antenna theory and design*. John Wiley & Sons, 2012.

[46] A. H. Lokman, P. J. Soh, S. N. Azemi, H. Lago, S. K. Podilchak, S. Chalermwisutkul, M. F. Jamlos, A. A. Al-Hadi, P. Akkaraekthalin, and S. Gao, "A review of antennas for picosatellite applications," *International Journal of Antennas and Propagation*, vol. 2017, 2017.

[47] J. Costantine, Y. Tawk, I. Maqueda, M. Sakovsky, G. Olson, S. Pellegrino, and C. G. Christodoulou, "Uhf deployable helical antennas for cubesats," *IEEE Transactions on Antennas and Propagation*, vol. 64, no. 9, pp. 3752–3759, 2016.

[48] D. Ochoa, K. Hummer, and M. Ciffone, "Deployable helical antenna for nanosatellites," in *28th Annual AIAA/USU Conference on Small Satellite*, 2014.

[49] Semtech Corporation, "SX1276/77/78/79 - 137 MHz to 1020 MHz Low Power Long Range Transceiver," Mar. 2015.

[50] A. V. Oppenheim and R. W. Schafer, *Discrete-Time Signal Processing*. Englewood Cliffs, New Jersey: Prentice-Hall, 1989.

Acknowledgements

The work presented in this thesis is the outcome of three “eventful” but beautiful years spent into the *Pal. 2* (the building with the capital P), and it has been accomplished thanks to the help of several people I had the pleasure to collaborate with.

Obviously you are the first, Giulio, heartfelt thanks for giving me the opportunity to join the SPADiC Lab and many many thanks for your constant support during my whole Ph.D. It was nice to work with you!!!

Another huge thanks goes to my diving instructor Tommy, which helped and followed me during my “misadventures” like a GPS data logger tracks a shipping ;)

I am also thankful to my colleagues Michi and Ale for the jokes and the gags that, despite many problems occurred in our office every year, made it a great environment where work. These guys have been an invaluable help when the job became *aaah... too difficult!! Beef?*

Last but non least, the *ottici* of “the gang of black coffee”, with which I drank the worst coffees of my life, but cheered by the music of Lucio Dalla at $\lambda = 1550$ nm in the background. Ehi, I was just kidding, the coffees was not so bad (I would rather avoid paying 30€ for some complaint for defamation).

I will miss you all so much, I hope to see you soon again!!!!